Optimal Threshold Design for Quanta Image Sensor

Omar A. Elgendy, *Student Member, IEEE* and Stanley H. Chan, *Member, IEEE*

arXiv:1704.03886v1 [cs.CV] 12 Apr 2017

***Abstract*—Quanta Image Sensor (QIS) is a binary imaging device envisioned as a candidate for the next generation image sensor after CCD and CMOS. Equipped with a massive number of single photon detectors, the sensor has a threshold q above which the number of arriving photons will trigger a binary response "1". Existing methods in the device literature typically assume that $q = 1$ for circuit simplicity. We argue that a spatially varying threshold can significantly improve the signal to noise ratio of the reconstructed image. In this paper, we present an optimal threshold design method. We make two contributions. First, we derive a set of oracle threshold results to inform the maximally achievable performance. We show that the oracle threshold should match exactly with the underlying pixel intensity. Second, we show that around the oracle threshold there exists a set of thresholds that give asymptotically unbiased reconstructions. The asymptotic unbiasedness has a phase transition behavior which allows us to develop a practical threshold update scheme using a bisection method. Experimentally, the new threshold design method achieves better rate of convergence than existing methods.**

***Index Terms*—Quanta image sensor, threshold adaptation, high dynamic range, quantization map, maximum likelihood.**

I. Introduction

A. Threshold Design for Quanta Image Sensor

Quanta Image Sensor (QIS) is a class of solid-state image sensors envisioned as the next generation imaging device after CCD and CMOS. Originally proposed by Eric Fossum in 2005 [1], the sensor has gained significant momentum in the past decade, both in terms of hardware design [2]–[4] and image processing [5]–[9]. The advantage of QIS over the mainstream CCD and CMOS is attributed to its high spatial resolution (e.g., 10^9 pixels per sensor with 200nm pitch per pixel [10]) and high speed (e.g., 100k fps as reported in [11]). However, in order to simplify its circuit, minimize power consumption and reduce the amount of data transfer, QIS is operated in a binary mode: When the number of photons arriving at the sensor exceeds a threshold q, the sensor generates a binary bit "1". When the number of photons is less than q, the sensor generates a "0". The goal of this paper is address the question of how to optimally choose q.

Optimal threshold design for QIS is important as it directly affects the dynamic range of an image. Figure 1 illustrates an example. In this figure, we simulate the raw binary data acquired by a QIS using certain threshold q. When q is low, most of the bits in the raw input are "1". The reconstructed image is therefore an over-exposed image. On the other hand, when q is high, most of the bits in the raw input are "0". The reconstructed image is then under-exposed. In either case, the simulation result illustrates the fact that a constant threshold has a limited performance. We argue that a better way is to allow q to vary spatially so that a pixel (or a group of pixels) has its own threshold value. By optimally determining the thresholds we can maximize the signal-to-noise ratio and the dynamic range of the reconstructed image.

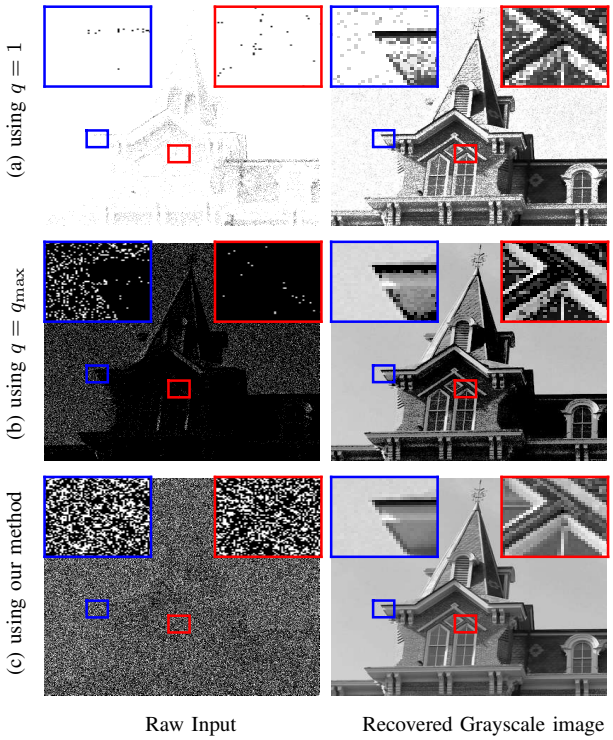

Fig. 1. Simulated QIS data and the reconstructed gray-scale images. In this experiment, we spatially oversample each pixel by $K = 2 \times 2 = 4$ binary bits and we use $T = 13$ independent temporal measurements.

B. Scope and Contributions

The goal of this paper is to present an optimal threshold design methodology. We make two contributions.

First, we provide a rigorous theoretical analysis of the performance limit of the image reconstruction as a function of the threshold. These results form the basis of our subsequent discussions of the threshold update scheme. Some results are known previously, e.g., the signal to noise ratio is a function of the Fisher Information [16], [17]. Several new results are established: (i) We show that the maximum likelihood estimate has a closed-form expression in terms of the incomplete Gamma function (Section III.B); (ii) We show that the oracle threshold can be derived in closed-form by maximizing the signal to noise ratio (Section III.C); (iii) We show that the image reconstruction has a phase transition behavior (Section IV.A - Section IV.B).

The authors are with the School of Electrical and Computer Engineering, Purdue University, West Lafayette, IN 47907, USA. Email: { oelgendy, stanchan}@purdue.edu.

This paper follows the concept of reproducible research. All the results and examples presented in the paper are reproducible using the code and images available online at http://engineering.purdue.edu/ChanGroup/.

TABLE I
LIST OF QIS PROTOTYPES AND PARAMETERS

Camera	Canon 5D CMOS	EMCCD [12]	GMAPD [13]	SPC SPAD [14]	SwissSPAD [11]	Fossum QIS [15]
Price	$\$5,000$	$\$20,000$	Prototype	Prototype	Prototype	Prototype
Resolution	4096×2160	1024×1024	256×256	320×240	512×128	1376×768
Pixel Pitch (μm)	6.25	13	25	8	24	3.6
Full-well capacity	69 ke- (@ISO100)	80 ke-	-	$56 - 125$ e-	-	$1 - 250$ e-
Frames per second (fps)	6	$26 - 92$	8×10^3	2×10^4	1.56×10^5	1×10^3
Sensor data rate	88.6 Mbps	0.48 Gbps	0.52 Gbps	1.54 Gbps	10.24 Gbps	1 Gbps

Second, we propose an efficient threshold update scheme based on our theoretical results. The new scheme adopts a bisection method which iteratively updates the threshold *without* the need of reconstructing the image. By checking whether the proportion of one's and zero's approaches 0.5 in a spatial-temporal block, the threshold is guaranteed to be near optimal. Compared to other existing threshold update schemes such as [18] and [19]–[21], the new scheme offers significantly faster rate of convergence (Section IV.C). We also demonstrate how the dynamic range can be extended for high dynamic range (HDR) imaging (Section IV.D).

The preliminary work of this paper was presented in ICIP 2016 [8]. This journal version contains significantly more details. In particular, we provide complete proofs of major results. We make comprehensive comparisons with existing methods and we include discussions of HDR imaging.

II. BACKGROUND

A. Current State of QIS

Quanta Image Sensor (QIS) belongs to the family of photon-counting devices. Photon-counting devices have been known for a long time. Examples include electron-multiplying charge-coupled device (EMCCD) [22], [23], single-photon avalanche diode (SPAD) [11], [14], [24], Geiger-mode avalanche photodiode (GMAPD) [13], etc. The common feature of these devices is their single photon sensitivity. Many of these devices are used in medical imaging [25]–[27], astronomy [28], defense [29], nuclear engineering [30], depth and reflectivity reconstruction [31], and recently in quantum random number generation used in cryptography [32], [33].

The concept of QIS was first proposed by Fossum in 2005 as a solution for sub-diffraction limit pixels. The sensor was called the digital film sensor, and later the quanta image sensor [15], [34], [35]. After the introduction of QIS, researchers in EPFL developed a similar concept called the Gigavision camera [6], [36], [37]. Recently, teams at the University of Edingburgh [14], [24], [38] and EPFL [32], [39] have made new progresses in QIS using binary single photon detectors. In the industry, Rambus Inc. (Sunnyvale, CA) has developed binary image sensors for high dynamic range imaging [19]–[21]. Table I lists several recent QIS prototypes that are available or are currently being developed. As a comparison we also show a Canon 5D Mark III CMOS camera. Among many different features, the most noticeable is the frame rate. For example, SPS SPAD can be operated at 20k fps. SwissSPAD can even achieve 156k fps. Both are significantly faster than a standard CMOS camera.

B. Related Work on Threshold Design

Existing work on QIS threshold design study can be summarized into two classes of methods.

- Markov Chain [18]. The Markov Chain method developed by Hu and Lu [18] is a time-sequential update scheme. A Markov Chain probability is used to control how easy the threshold should be increased or decreased. While the method has provable convergence, the threshold of each single photon detector of the QIS has to be updated sequentially in time. In contrast, our proposed method allows a group of single photon detectors to share the same threshold. As a result, our proposed method has significantly faster rate of convergence.
- Conditional Reset [19]–[21]. The conditional reset method is a hardware solution proposed by Vogelsang and colleagues. The idea is to take a sequence of images with ascending (or descending) thresholds, and digitally integrate the sequence to form an image. The drawback of the method, besides the additional hardware cost of the per-pixel reset transistors, is the limited quality of the reconstructed image. For the same number of frames, our proposed method produces better images.

C. QIS Imaging Model

In this subsection we provide an overview of the QIS imaging model. The model has been previously discussed in several papers, e.g., [6]–[9]. Readers interested in details can refer to these papers for further explanations.

1) Spatial Oversampling: We denote the discrete version of the light intensity as a vector $\boldsymbol{c} = [c_0, \ldots, c_{N-1}]^T$, where $n = 0, \ldots, N-1$ specify the spatial coordinates. We assume that c_n is normalized to the range $[0, 1]$ for all n so that there is no scaling ambiguity. To model the actual light intensity, we multiply c_n by a constant α to yield αc_n, where $\alpha > 0$ is a fixed scalar constant.

Given the N-dimensional vector $\boldsymbol{c}$, QIS uses $M \gg N$ tiny pixels called *jots* to sample $\boldsymbol{c}$. The ratio $K \stackrel{\text{def}}{=} M/N$ is known as the spatial oversampling factor. The oversampling process is illustrated in Figure 2, where it first upsamples the vector $\boldsymbol{c}$ by a factor of K, and then filters the output by a lowpass filter $\{g_k\}$. Mathematically, the process can be expressed as

$$\boldsymbol{\theta} = \alpha \boldsymbol{G} \boldsymbol{c}, \tag{1}$$

where $\boldsymbol{\theta} = [\theta_0, \ldots, \theta_{M-1}]^T$ denotes the light intensity sam-

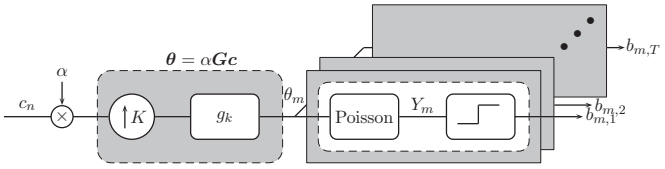

Fig. 2. Block diagram illustrating the image formation process of QIS.

pled at the M jots, and the matrix $\boldsymbol{G}$ is defined as

$$\boldsymbol{G} = \frac{1}{K} \boldsymbol{I}_{N\times N} \otimes \mathbf{1}_{K\times 1}, \tag{2}$$

where $\mathbf{1}_{K\times 1}$ is a vector of all ones and $\otimes$ denotes the Kronecker product. Note that the choice of $\boldsymbol{G}$ in (2) is the result of a simplified model by assuming that the lowpass filter is $g_k = 1/K$ for all k. It is possible to use a general lowpass filter as discussed in [6], [7]. However, in order to simplify the theoretical derivation, we will focus on this special $\boldsymbol{G}$.

2) Truncated Poisson Process: We assume that the operating speed of QIS is significantly faster than the scene motion. Therefore, for a given scene $\boldsymbol{c}$ (and also $\boldsymbol{\theta}$), we are able to acquire a set of T independent measurements. We illustrate this using the T channels in Figure 2.

The oversampled signal $\boldsymbol{\theta}$ generates a sequence of Poisson random variables according to the distribution

$$\mathbb{P}(Y_{m,t} = y_{m,t}) = \frac{\theta_m^{y_{m,t}} e^{-\theta_m}}{y_{m,t}!}, \tag{3}$$

where $m = 0, 1, \ldots, M-1$ denotes the m-th jot of the QIS and $t = 0, 1, \ldots, T-1$ denotes the t-th independent measurement in time. Denoting $q \in \mathbb{N}$ as the quantization threshold, the final observed binary measurement $B_{m,t}$ is a truncation of $Y_{m,t}$:

$$B_{m,t} = \begin{cases} 0, & \text{if } Y_{m,t} < q. \\ 1, & \text{if } Y_{m,t} \geq q \end{cases}$$

The probability mass function of $B_{m,t}$ is given by

$$\mathbb{P}(B_{m,t} = b_{m,t}) = \begin{cases} \sum\limits_{k=0}^{q-1} \frac{\theta_m^k e^{-\theta_m}}{k!}, & \text{if } b_{m,t} = 0, \\ \sum\limits_{k=q}^{\infty} \frac{\theta_m^k e^{-\theta_m}}{k!}, & \text{if } b_{m,t} = 1. \end{cases} \tag{4}$$

3) Properties of Truncated Poisson Processes: The probability mass function of $B_{m,t}$ in (4) shows that $B_{m,t}$ is a Bernoulli random variable. However, the right hand side of (4) involves an infinite sum which is difficult to interpret. To alleviate the infinite sum, we consider the upper incomplete Gamma function $\Psi_q : \mathbb{R}^+ \to [0, 1]$ defined in [40] as:

$$\Psi_q(\theta) \stackrel{\text{def}}{=} \frac{1}{\Gamma(q)} \int_\theta^\infty t^{q-1} e^{-t} dt, \quad \text{for } \theta > 0,\ q \in \mathbb{N}.$$

where $\Gamma(q) = (q-1)!$ is the standard Gamma function. The incomplete Gamma function allows us to rewrite the infinite sum in (4) as follows:

$$\Psi_q(\theta) = \sum_{k=0}^{q-1} \frac{\theta^k}{k!} e^{-\theta}. \tag{5}$$

Consequently, the probabilities in (4) become

$$\begin{aligned} \mathbb{P}(B_{m,t} = 0) &= \Psi_q(\theta_m), \\ \mathbb{P}(B_{m,t} = 1) &= 1 - \Psi_q(\theta_m). \end{aligned} \tag{6}$$

Example 1. *In the special case of $q = 1$, we obtain:*

$$\mathbb{P}(B_{m,t} = 0) = \frac{1}{\Gamma(1)} \int_{\theta_m}^\infty t^0 e^{-t} dt = e^{-\theta_m},$$

which coincides with the results shown in [6] and [7].

The incomplete Gamma function $\Psi_q(\theta)$ is a decreasing function of θ because the first order derivative of $\Psi_q(\theta)$ with respect to θ is negative:

$$\frac{d}{d\theta} \Psi_q(\theta) = \frac{-\theta^{q-1} e^{-\theta}}{\Gamma(q)} < 0, \quad \forall q \in \mathbb{N}, \text{ and } \theta > 0. \tag{7}$$

The limiting behavior of $\Psi_q(\theta)$ is important. For a fixed q, the function $\Psi_q(\theta) \to 1$ as $\theta \to 0$ and $\Psi_q(\theta) \to 0$ as $\theta \to \infty$. While Ψ_q^{-1} still exists in these situations because Ψ_q is monotonically decreasing, for a given z the value $\Psi_q^{-1}(z)$ could be numerically very difficult to evaluate. To characterize the sets of θ and q that Ψ_q is (numerically) invertible, we define the *θ-admissible set* and the *q-admissible set*.

Definition 1. *The* θ-admissible set *and* q-admissible set *of the incomplete Gamma function are*

$$\begin{aligned} \Theta_q &\stackrel{def}{=} \{\theta \mid \varepsilon \leq \Psi_q(\theta) \leq 1 - \varepsilon\}, \\ \mathcal{Q}_\theta &\stackrel{def}{=} \{q \mid \varepsilon \leq \Psi_q(\theta) \leq 1 - \varepsilon\}, \end{aligned} \tag{8}$$

respectively, where $0 < \varepsilon < 1$ is a constant.

More discussions of the incomplete Gamma function can be found in the Supplementary material.

III. Optimal Threshold: Theory

In this section we present a set of oracle results.

A. Image Reconstruction by MLE

We begin by discussing image reconstruction because the optimality of the threshold is measured with respect to the reconstructed image. The goal of image reconstruction is to recover the underlying image $\boldsymbol{c}$ from the binary measurements $\mathcal{B} = \{B_{m,t} \mid m = 0, \ldots, M-1, \text{and } t = 0, \ldots, T-1\}$. Image reconstruction for QIS is a known problem and there are several existing methods, such as gradient descent [6], dynamic programming [41], ADMM [7], and Transform-Denoise method [9]. In order to ensure analytic tractability, we shall focus on the maximum likelihood estimation (MLE) approach, which has a closed-form expression.

Given $\mathcal{B}$, MLE solves the following optimization problem:

$$\begin{aligned} \widehat{\boldsymbol{c}} &\stackrel{(a)}{=} \underset{\boldsymbol{c}}{\text{argmax}} \prod_{t=0}^{T-1} \prod_{m=0}^{M-1} \mathbb{P}[B_{m,t} = 1\,;\, \theta_m]^{b_{m,t}} \\ &\qquad \times \mathbb{P}[B_{m,t} = 0\,;\, \theta_m]^{1-b_{m,t}} \\ &\stackrel{(b)}{=} \underset{\boldsymbol{c}}{\text{argmax}} \sum_{t=0}^{T-1} \sum_{m=0}^{M-1} \Big\{ b_{m,t} \log(1 - \Psi_q(\theta_m)) \\ &\qquad + (1 - b_{m,t}) \log \Psi_q(\theta_m) \Big\}, \end{aligned} \tag{9}$$

subject to the constraint that $\boldsymbol{\theta} = \alpha \boldsymbol{G} \boldsymbol{c}$. Here, the right hand side of (a) is the likelihood function of a Bernoulli

random variable, and (b) follows from taking the logarithm. With the $\boldsymbol{G}$ defined in (2), we can partition $\mathcal{B}$ into N blocks $\{\mathcal{B}_1, \ldots, \mathcal{B}_N\}$ where each block is

$$\mathcal{B}_n \overset{\text{def}}{=} \{B_{Kn+k,t} \mid k = 0, \ldots, K-1, t = 0, \ldots, T-1\}.$$

Then, the pixel $\widehat{c}_n$ can be estimated as follows.

Proposition 1 (Closed-form ML Estimate)**.** *The solution of the MLE in* (9) *is*

$$\widehat{c}_n = \frac{K}{\alpha} \Psi_q^{-1} \left(1 - \frac{S_n}{KT}\right), \tag{10}$$

where $S_n \overset{def}{=} \sum_{t=0}^{T-1} \sum_{k=0}^{K-1} B_{Kn+k,t}$ *is the sum of bits in the* n*-th block* $\mathcal{B}_n$*.*

Proof: See [9]. ∎

B. Signal-to-Noise Ratio of ML Estimate

In order to determine the optimal threshold, we need to quantify the performance of the ML estimate. The performance metric we use is the signal-to-noise ratio of the ML estimate at every pixel $\widehat{c}_n$. Considering each $\widehat{c}_n$ individually is allowed here because they are independently determined according to (10). For notation simplicity we drop the subscript n in the subsequent discussions.

Definition 2. *The signal-to-noise ratio (SNR) of the ML estimate* $\widehat{c}$ *is defined as*

$$\mathrm{SNR}_q(c) \overset{def}{=} 10 \log_{10} \frac{c^2}{\mathbb{E}[(\widehat{c} - c)^2]}, \tag{11}$$

where the expectation is taken over the probability mass function of the binary measurements in (6)*.*

The difficulty of working with $\mathrm{SNR}_q(c)$ is that it does not have a simple closed-form expression. In view of this, Lu [17] showed that the SNR is asymptotically linear to the log of the Fisher Information.

Proposition 2. *As* $KT \to \infty$*,*

$$\mathrm{SNR}_q(c) \approx 10 \log_{10} \left(c^2 I_q(c)\right) + 10 \log_{10} KT, \tag{12}$$

where $I_q(c)$ *is the Fisher Information of the probability mass function defined in* (6)*.*

Proof: See [17]. ∎

While the asymptotic result shown in Proposition 2 has significantly simplified the SNR, we still need to determine the Fisher Information. The following proposition gives a new result of the Fisher Information with arbitrary q.

Proposition 3. *The Fisher Information* $I_q(c)$ *of the probability mass function in* (6) *under a threshold* q *is:*

$$I_q(c) = \left(\frac{\alpha}{K}\right)^2 \frac{e^{-2\left(\frac{\alpha c}{K}\right)} \left(\frac{\alpha c}{K}\right)^{2q-2}}{\Gamma^2(q) \Psi_q\left(\frac{\alpha c}{K}\right)\left(1 - \Psi_q\left(\frac{\alpha c}{K}\right)\right)}. \tag{13}$$

Proof: See Appendix A-A. ∎

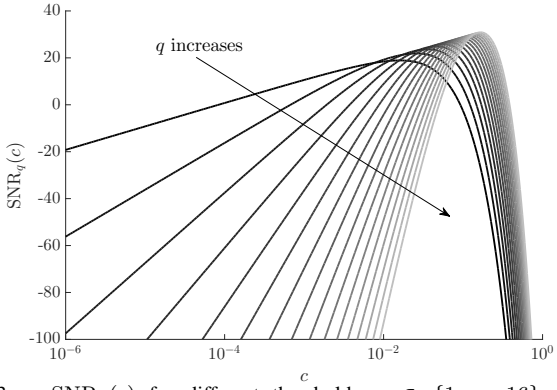

Fig. 3. $\mathrm{SNR}_q(c)$ for different thresholds $q \in \{1, \ldots, 16\}$. In this experiment, we set $\alpha = 400$, $K = 4$, and $T = 30$. For fixed q, $\mathrm{SNR}_q(c)$ is always a convex function.

Substituting (13) into (12), we observe that the SNR can be approximated as

$$\mathrm{SNR}_q(c) \approx 10 \log_{10} \frac{KT e^{-2\left(\frac{\alpha c}{K}\right)} \left(\frac{\alpha c}{K}\right)^{2q}}{\Gamma(q)^2 \Psi_q\left(\frac{\alpha c}{K}\right)\left(1 - \Psi_q\left(\frac{\alpha c}{K}\right)\right)}, \tag{14}$$

which is characterized by the unknown pixel value c, the threshold q, the spatial oversampling ratio K and the number of temporal measurements T. To understand the behavior of (14), we show in Figure 3 $\mathrm{SNR}_q(c)$ as a function of c for different thresholds $q \in \{1, \ldots, 16\}$. For a fixed q, $\mathrm{SNR}_q(c)$ is a convex function with a unique maximum. The goal of optimal threshold design is to determine a q which maximizes $\mathrm{SNR}_q(c)$ for a fixed c.

Remark 1. *The* $\mathrm{SNR}_q(c)$ *in* (14) *can also be derived from a concept in the device literature called the* exposure-referred SNR *[42]. See Supplementary material for discussions.*

C. Oracle Threshold

We now discuss the optimal threshold design in an oracle setting. We call the result oracle because the optimal threshold depends on the unknown pixel intensity c. The practical threshold design scheme will be discussed in Section IV.

Using the definition of the signal-to-noise ratio, the optimal threshold is determined by maximizing $\mathrm{SNR}_q(c)$ with respect to q:

$$q^* = \underset{q \in \mathbb{N}}{\operatorname{argmax}} \ \mathrm{SNR}_q(c) = \underset{q \in \mathbb{N}}{\operatorname{argmax}} \ \log(c^2 I_q(c)). \tag{15}$$

The second equality follows from Proposition 2. Substituting (13) yields an expression of the right hand side of (15). To further simplify the expression we derive the following lower bound.

Proposition 4. *The function* $\log(c^2 I_q(c))$ *is lower bounded as follows.*

$$\log(c^2 I_q(c)) \geq \underbrace{2\left(\log 2 - \frac{\alpha c}{K} + q \log \frac{\alpha c}{K} - \log \Gamma(q)\right)}_{\overset{def}{=} L_q(c)}.$$

Proof: See Appendix A-B. ∎

Using this lower bound, we can derive the optimal threshold q as follows.

Proposition 5. *The optimal threshold $q^*(c)$ is*

$$q^*(c) = \underset{q\in\mathbb{N}}{\text{argmax}}\ L_q(c) = \left\lfloor \frac{\alpha c}{K} \right\rfloor + 1, \tag{16}$$

where $\lfloor\cdot\rfloor$ denotes the flooring operator that returns the largest integer smaller than or equal to the argument.

Proof: See Appendix A-C. ∎

The result of Proposition 5 is important. It states that the oracle threshold is exactly the same as the light intensity observed at a jot, i.e., $\alpha c/K$. The flooring operation and the addition of a constant 1 ensure that the threshold is an integer. In fact, a special where $\alpha = 1$ has been experimentally demonstrated in [18]. The new result in Proposition 5 provides a theoretical justification.

IV. Optimal Threshold: Practice

The oracle threshold derived in the previous section provides a theoretical foundation but is practically not feasible. In this section, we present a practical threshold design that achieves a relaxed optimality criteria. The insight of the proposed method is drawn from the following asymptotic unbiasedness and phase transition phenomenon.

A. Asymptotic Unbiasedness

Recall in Proposition 1 we showed that for a spatial-temporal block $\mathcal{B}_n$, the maximum likelihood (ML) estimate $\widehat{c}$ has to satisfy the condition

$$\Psi_q\left(\frac{\alpha\widehat{c}}{K}\right) = 1 - \frac{S}{KT}, \tag{17}$$

where $S = \sum_{t,k} B_{Kn+k,t}$ is the sum of bits in $\mathcal{B}_n$. We define the right hand side of the equation as

$$\gamma_q(c) \overset{\text{def}}{=} 1 - \frac{S}{KT}. \tag{18}$$

In the device literature (e.g., [42]), the term $1-\gamma_q(c)$ is known as the *bit-density* as it is the proportion of ones in $\mathcal{B}_n$.

There are a few important properties about $\gamma_q(c)$. First of all, $\gamma_q(c)$ is a random variable. The mean and variance of $\gamma_q(c)$ are given by the following proposition.

Proposition 6. *The mean and variance of $\gamma_q(c)$ are*

$$\begin{aligned}\mathbb{E}[\gamma_q(c)] &= \Psi_q\left(\frac{\alpha c}{K}\right), \ \textit{and}\\ \text{Var}[\gamma_q(c)] &= \frac{1}{KT}\Psi_q\left(\frac{\alpha c}{K}\right)\left[1-\Psi_q\left(\frac{\alpha c}{K}\right)\right],\end{aligned} \tag{19}$$

respectively.

Proof: See Appendix A-D. ∎

Applying strong law of large number to $\gamma_q(c)$, we show that

$$\gamma_q(c) \overset{a.s.}{\to} \mathbb{E}[\gamma_q(c)] = \Psi_q(\alpha c/K), \tag{20}$$

as $KT \to \infty$. As a result, the ML estimate $\widehat{c}$, which is also a random variable, should have its mean $\mathbb{E}[\widehat{c}]$ converging to c:

$$\mathbb{E}[\widehat{c}] \overset{(a)}{=} \frac{K}{\alpha}\mathbb{E}\left[\Psi_q^{-1}\left(\gamma_q(c)\right)\right] \overset{(b)}{\to} \frac{K}{\alpha}\mathbb{E}\left[\Psi_q^{-1}\Psi_q\left(\frac{\alpha c}{K}\right)\right] \overset{(c)}{=} c.$$

In the above derivation, (a) follows from the definition of $\widehat{c}$, (b) follows from (20), and (c) holds because Ψ_q and Ψ_q^{-1} cancel each other.

The result we have just shown is the asymptotic unbiasedness of the ML estimate $\widehat{c}$. Asymptotic unbiasedness means that as the number of independent measurements grows, the ML estimate $\widehat{c}$ approaches to the ground truth c. In other words, as long as KT is large enough, the random variable $\widehat{c}$ would be a very good estimate of the ground truth.

Does an asymptotically unbiased estimate maximize the SNR? The answer is no, because Proposition 5 states that if q^* is the optimal threshold, then $\text{SNR}_{q^*}(c) \geq \text{SNR}_q(c)$ for any $q \neq q^*$. Therefore, moving from the exact optimal q^* to a threshold that leads to an asymptotically unbiased estimate is a relaxation of the optimality criteria.

In order to understand the difference between the two optimality criteria, we make a quick detour to first understand the limitation of the incomplete Gamma function. For finite KT, it is possible that $\gamma_q(c) = 0$ or $\gamma_q(c) = 1$, i.e., all bits in $\mathcal{B}_n$ are 1's or 0's. When either case happens, the inversion of the incomplete Gamma function becomes problematic because every incomplete Gamma function has a q-admissible set $\mathcal{Q}_\theta$ (See Definition 1). Putting into the QIS problem, the tolerance level ε defining $\mathcal{Q}_\theta$ should be set as follows.

Proposition 7. *Let $0 < \delta < 1$ be a constant. Then, for any*

$$q \in \mathcal{Q}_\theta \overset{def}{=} \left\{ q \,\middle|\, 1 - \left(\frac{\delta}{2}\right)^{\frac{1}{KT}} \leq \Psi_q(\theta) \leq \left(\frac{\delta}{2}\right)^{\frac{1}{KT}} \right\}, \tag{21}$$

the random variable $\gamma_q(c)$ will not attain a value of 0 or 1 with probability at least $1-\delta$, i.e.,

$$\mathbb{P}[0 < \gamma_q(c) < 1] > 1 - \delta.$$

Proof: See Appendix A-E. ∎

Example 2. *We consider an example to illustrate the magnitude of the quantities in Proposition 7. In this example, we let the ground truth pixel value be $c = 0.5$. The sensor parameters are set as $T = 50$, $K = 4$, $\alpha = 300$. For a constant $\delta = 2\times10^{-4}$, the tolerance level is $\varepsilon = 1 - (\delta/2)^{1/KT} = 0.045$. Therefore, as long as $q \in \{q \,|\, 0.045 \leq \Psi_q(\theta) \leq 1 - 0.045\}$, which is the set $\{q \mid 28 \leq q \leq 48\}$, the probability that $\gamma_q(c)$ equals to 0 or 1 is upper bounded by $\delta = 2\times10^{-4}$.*

B. Phase Transition Phenomenon

The combination of the above asymptotic unbiasedness and the q-admissibility of the incomplete Gamma function leads to an important phenomenon. Figure 4 shows the plot of a typical experiment with experimental setup discussed in Example 2. We generate 10,000 random realizations, where each realization is a spatial-temporal block $\mathcal{B}_n$ containing $KT = 200$ binary bits. In the plot, we show the average bit density $1 - \gamma_q(c)$. This average is taken over the 10,000 realizations. We also overlay the average with the true expectation $1-\Psi_q(\theta)$ (where $\theta = \alpha c/K$) to verify the validity of our equations. In the same plot, we mark the q-admissible set $\mathcal{Q}_\theta$ with the tolerance level ε calculated in Example 2.

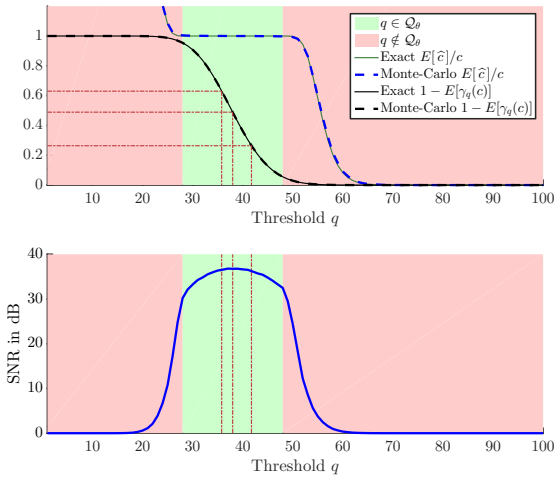

Fig. 4. Phase transition of the ML estimate and its relationship to the average bit density $1 - \mathbb{E}[\gamma_q(c)]$. The red region is where it is impossible to recover c, whereas the green region is where we can have perfect recovery.

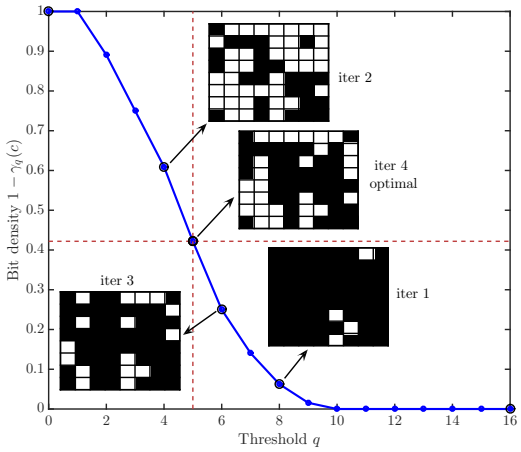

Fig. 5. The proposed bisection update scheme adjusts the threshold q such that the bit density $1 - \gamma_q(c)$ approaches 0.5. The iteration illustrates the bisection steps.

The asymptotic unbiasedness of $\widehat{c}$ can be understood from the ratio $\mathbb{E}[\widehat{c}]/c$. Let $\mathcal{Q}_\theta = \{q \mid q_L \le q \le q_H\}$, where q_L and q_H are the smallest and the largest integers in $\mathcal{Q}_\theta$ respectively. There are three distinct phases:

- When $q < q_L$, the threshold is low and so most bits become 1. Therefore, $\gamma_c(q) \to 0$ and hence $\widehat{c} \to \infty$. Thus, $\mathbb{E}[\widehat{c}]/c \to \infty$ as q decreases.
- When $q > q_H$, the threshold high and so most bits become 0. Therefore, $\gamma_c(q) \to 1$ and hence $\widehat{c} \to 0$. Thus, $\mathbb{E}[\widehat{c}]/c \to 0$ as q increases.
- When $q_L \le q \le q_H$, the ML estimate $\widehat{c}$ is asymptotically unbiased. Therefore, $\mathbb{E}[\widehat{c}]/c = 1$.

These three phases are indicated by the coloring in Figure 4.

We can now come back to the question of how an asymptotically unbiased estimate is compared to the oracle estimate. Or more precisely, how much SNR drop will there be if we choose a $q \in \mathcal{Q}_\theta$ but not necessarily $q = q^*$? As shown in Figure 4, $\mathrm{SNR}_q(c)$ stays close to $\mathrm{SNR}_{q^*}(c)$ if q is close to q^*. However, as q moves away from q^*, the average bit density $1 - \mathbb{E}[\gamma_c(q)]$ also changes. This is a very useful phenomenon, because now we can control q to aim for a specific level of the average bit density. For example, in the case of Figure 4, we observe that for a set of q such that $0.25 \le 1 - \mathbb{E}[\gamma_q(c)] \le 0.6$ (which is reasonably wide), the SNR stays in the range $36.15\mathrm{dB} \le \mathrm{SNR}_q(c) \le 36.65\mathrm{dB}$ (which is reasonably narrow). In practice, we observe that as long as q is chosen to ensure $\gamma_c(q) \approx 0.5$, the final SNR is close to the optimal SNR.

Choosing the level 0.5 can be justified from an information theoretic perspective. The goal of threshold update is to find a q such that the information available in $\mathcal{B}_n$ is maximized. When q is too high or too low, information is lost because most bits are either 1 or 0. The entropy is maximized when the probability of obtaining a zero and the probability of obtaining a one is equal, i.e., 0.5. Additional discussions of the choice of 0.5 and the variation of $\mathrm{SNR}_q(c)$ can be found in the Supplementary material.

Algorithm 1 Bisection Threshold Update Scheme

Initial thresholds q_A and q_B such that $1 - \gamma_{q_A} > 0.5$ and $1 - \gamma_{q_B} < 0.5$.
Compute $q_M = \lceil (q_A + q_B)/2 \rceil$, where $\lceil \cdot \rceil$ denotes the ceiling operator.
while $|\gamma_{q_M} - 0.5| < \texttt{tol}$ **do**
  If $\gamma_{q_M} < 0.5$, then set $q_A = q_M$. Else, set $q_B = q_A$.
  Compute $q_M = \lceil (q_A + q_B)/2 \rceil$.
end while
return q_M

C. Bisection Threshold Update Scheme

The above analysis of the ML estimate leads to our proposed threshold update scheme. The idea is to make sure that the measured bit density $\gamma_q(c)$ stays close to 0.5. To achieve this goal, we propose a bisection method illustrated in Figure 5 and Algorithm 1. Starting with initial thresholds q_A and q_B, we check whether the bit density satisfies $1 - \gamma_{q_A} > 0.5$ and $1 - \gamma_{q_B} < 0.5$. If this is the case, then we find a mid point $q_M = (q_A + q_B)/2$ and check whether $1 - \gamma_{q_M}$ is greater or less than 0.5. If $1 - \gamma_{q_M} > 0.5$, we replace q_A by q_M, otherwise we replace q_B by q_M. The process repeats until $1 - \gamma_{q_M}$ is sufficiently close to 0.5.

In our proposed threshold update scheme, we assume that the image has been partitioned into N blocks $\{\mathcal{B}_n \mid n = 1, \ldots, N\}$. Each $\mathcal{B}_n$ contains KT binary bits and is used to estimate one pixel value c_n. This setting results in N different thresholds, one for every pixel. To generalize the setting, it is also possible to allow multiple pixels to share a common threshold. Figure 6 shows an example. The advantage of sharing threshold for multiple pixels is that circuits associated with the sensor can be simplified. In terms of performance, since neighboring pixels are typically correlated, sharing the threshold causes little drop in the resulting SNR.

The price that the proposed bisection algorithm has to pay is the number of frames it requires to determine a good q. For every evaluation of γ_{q_M}, the sensor has to physically acquire one frame and compute the bit density in each of the

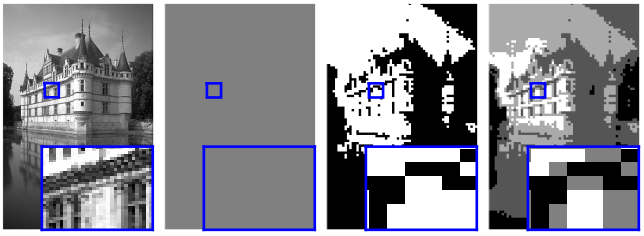

(a) scene (b) q at iter 1 (c) q at iter 2 (d) q at iter 3

Fig. 6. Threshold q at different iterations of the bisection algorithm. Note that q is spatially varying. In this example, one threshold value is shared by 16×16 jots. The maximum threshold level is $q_{\max} = 16$.

N blocks. Therefore, the more bisection steps we need, the more frames that the sensor has to physically acquire. The rate of convergence of the proposed method and existing methods will be compared in Section V.

D. Extension to High Dynamic Range

While QIS is a photon counting device, it is not designed to count an excessive number of photons. As a result, the maximum number of threshold levels is also limited. When using QIS for high dynamic range (HDR) imaging, appropriate dynamic range extension methods are needed.

We present two ways to enable QIS for HDR imaging:

- Reduce Duty Cycle. In the signal processing block diagram shown in Figure 2, we can replace the constant α by a fraction as $\alpha\tau$, where $0 \leq \tau \leq 1$ determines the duty cycle of each QIS exposure. For very bright scenes, a low duty cycle will prevent QIS from saturating early.
- Multiple Measurements. For dark scenes, multiple measurements can be taken to ensure enough photons over the measurement period. This, however, is different from conventional HDR imaging. In conventional HDR imaging, the multiple shots are taken at different shutter speeds, e.g., 1/8192, 1/2048, 1/512, 1/128, 1/32, 1/8, 1/2 seconds [43], which is redundant. QIS's multiple shot functions more similar to burst photography [44]. The amount of acquisition time is significantly less than the conventional HDR imaging.

Both methods can be used for *any* threshold scheme. The benefit of using our proposed threshold scheme is the amount of dynamic range extension it can support. In Figure 7, we illustrate the total dynamic range that can be covered using 4 multiple measurements at duty cycles $\tau = 1$, $\tau = 0.2$, $\tau = 0.04$, and $\tau = 0.008$. The maximum threshold level is $q_{\max} = 25$, and the minimum threshold level is $q_{\min} = 1$. It can be seen from the figure that with the optimal threshold q^*, the dynamic range is significantly more than the non-optimal ones. In particular, we observe a 16dB and a 54dB improvement compared to $q_{\min} = 1$ and $q_{\max} = 25$, respectively.

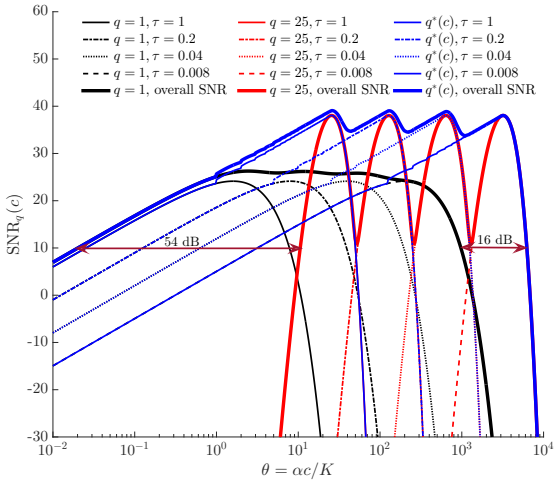
$q = 1, \tau = 1$
$q = 1, \tau = 0.2$
$q = 1, \tau = 0.04$
$q = 1, \tau = 0.008$
$q = 1$, overall SNR
$q = 25, \tau = 1$
$q = 25, \tau = 0.2$
$q = 25, \tau = 0.04$
$q = 25, \tau = 0.008$
$q = 25$, overall SNR
$q^*(c), \tau = 1$
$q^*(c), \tau = 0.2$
$q^*(c), \tau = 0.04$
$q^*(c), \tau = 0.008$
$q^*(c)$, overall SNR
54 dB
16 dB
$\mathrm{SNR}_q(c)$
$\theta = \alpha c/K$

Fig. 7. SNR in dB vs. exposure θ for HDR imaging mode obtained by fusion of frames with shutter duty cycles $\tau \in \{1, 0.2, 0.04, 0.008\}$. Three scenarios are shown: constant threshold with $q = 1$ (black), $q = 25$ (red) and an optimal spatially varying threshold (blue).

V. Experimental Results

In this section we evaluate the proposed threshold update scheme by comparing it with existing methods. We consider two evaluation metrics: (1) convergence rate of the threshold update methods; (2) quality of the reconstructed images. The dataset we use is the Berkeley segmentation and benchmark dataset [45], which contains 100 test images of resolution 481×321. We also test the threshold update scheme for high dynamic range images using the HDR-Eye dataset [46], [47]. In all experiments, we fix the spatial over-sampling factor as $K = 4 \times 4 = 16$, and number of temporal frames as $T = 13$. The maximum threshold level is set as $q_{\max} = 16$ to ensure that it is realistic for today's QIS.

A. Convergence

We compare the proposed threshold update scheme with the Markov Chain (MC) adaptation proposed by Hu and Lu [18]. The Markov Chain adaptation models the threshold as a variable with 2^L states. These 2^L states can be regarded as 2^L steps before reaching to the next threshold level. The probability of changing from one state to another is controlled by a parameter $1 - \beta$ with $0 < \beta < 1$. When a bit arrives, the state will be updated (increased or decreased) or will stay. Once the state is increased by 2^L times, the threshold will be increased by one.

When comparing Markov Chain adaptation with the proposed bisection algorithm, one should be aware of the difference between the two methods. Markov Chain adaptation is a *per-jot* update scheme whereas the proposed bisection algorithm is a *per-pixel* update scheme. For a pixel with $K \times K$ jots, Markov Chain adaptation needs K^2 iterations to update each jot *sequentially*. In contrast, the proposed bisection algorithm updates a common threshold for all K^2 jots *simultaneously*. Thus in practice our bisection algorithm is significantly less complex to implement in hardware than the Markov Chain. In order to take into account of the different forms of updates, we treat the K^2 iterations of Markov Chain adaptation as one "major iteration" and compare it with the one bisection step of the proposed algorithm.

The first comparison we make is to check the threshold at different jots. Figure 8 shows the results of three typical runs with ground truth threshold $q^* = 1, 8, 16$. In this experiment, we generate 100 random binary blocks of size $K \times K$ and

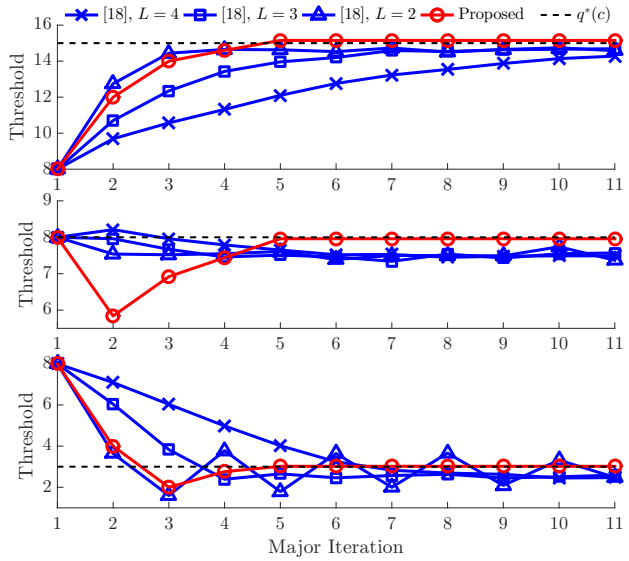

Fig. 8. Convergence of the threshold at 3 jots. Each curve is averaged over 100 random samples. The red curve indicates the proposed bisection method. The blue curves are the Markov chain adaptation [18] with $\beta = 0.25$. Note that one major iteration of Markov Chain adaptation corresponds to K^2 sequential updates, and one major iteration of the bisection method corresponds to a single update to K^2 jots simultaneously.

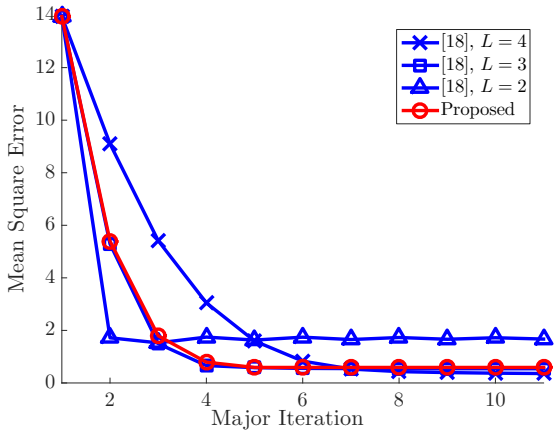

Fig. 9. Mean square error between the estimated threshold and the ideal oracle threshold. Each curve is averaged over 100 random samples and 100 testing images. The red curve indicates the proposed bisection method. The blue curves are the Markov chain adaptation [18] with $\beta = 0.25$.

estimate the threshold at each major iteration. We report the average of these 100 estimate to minimize the randomness of the data. The results show that one iteration of the proposed bisection algorithm works as good as the K^2 iterations of the Markov Chain adaptation. In some cases, Markov Chain tends to oscillate whereas the bisection result is stable.

The second comparison we make is to check how close the estimated threshold is compared to the optimal threshold. The optimal threshold q^* is obtained using the oracle scheme. In Figure 9, we plot the mean squared error between the estimated threshold and the oracle threshold. For fairness we show the results of the MSE average over all threshold values in the 100 images from the Berkeley segmentation dataset. One threshold is shared by $K \times K$ jots, and each $K \times K$ jots correspond to one pixel. The result is consistent with the ones shown in Figure 8.

TABLE II
AVERAGE PSNR AND STANDARD DEVIATION OF 100 RECOVERED IMAGES USING DIFFERENT Q-MAPS AND 50 RANDOM SAMPLES.

	Configuration	Average PSNR	Std
Fixed Threshold	$q = 1$	10.30	0.01
	$q = 5$	28.80	0.04
	$q = 10$	23.22	0.02
	$q = 16$	12.95	0.01
Conditional Reset [21]	Ascending q sequence	23.77	0.52
	Descending q sequence	24.95	0.53
Proposed Method	$2K^2 \times 2K^2$	30.14	0.06
	$K^2 \times K^2$	31.18	0.06
	$K \times K$	32.78	0.02

B. Image Reconstruction Quality

The convergence comparison in the previous subsection is only useful to compare threshold update methods that actually return a threshold. In the QIS literature, there are methods that implicitly update the threshold, e.g., the conditional reset method [21]. For comparison with these methods, we have to compare the quality of the image reconstructed from the binary raw data. The image reconstruction is done using the closed-form ML estimate in Section III-A.

We consider three classes of methods:

- Fixed Threshold. Fixed threshold is commonly used in the device literature [5]–[7]. A fixed threshold is a single threshold applied to all pixels in the image. In this experiment, we consider the following choices of fixed thresholds: $q = 1$, $q = 5$, $q = 10$ and $q = 16$.
- Conditional Reset [21]. Conditional reset counts the number of photons and is reset when it is above the threshold. The threshold in conditional reset is sequentially increasing or decreasing. The reconstructed image is obtained by digitally integrating the raw binary frames.
- Proposed Method. As we discussed in Section IV-C, the proposed method can be implemented to let multiple pixels share a common threshold. Thus, in this experiment we consider three sharing strategies: (1) Share a threshold between a neighborhood of $K \times K$ jots (i.e., one threshold for one pixel); (2) Share a threshold between a neighborhood of $K^2 \times K^2$ jots (i.e., one threshold for $K \times K$ pixel); (3) Share a threshold between a neighborhood of $2K^2 \times 2K^2$ jots (i.e., one threshold for $2K \times 2K$ pixels).

The result of the experiment is shown in Table II. The PSNR values reported are averaged over 100 testing images in the Berkeley segmentation dataset. Each image generates 50 random realizations, and the PSNR of an image is averaged over these 50 random realizations to minimize the randomness. As shown in the table, while conditional reset generally performs better than a fixed threshold, it performs significantly worse than the proposed threshold update scheme.

C. Influence of QIS Threshold on HDR Imaging

Since QIS does not have sufficient full well capacity to accumulate photons for HDR imaging, we apply the dynamic

Fig. 10. Bracketed images with different exposure settings. From Left to Right: -2.7,-2, -1.3, -0.7, 0, 0.7, 1.3, 2, and 2.7 EV.

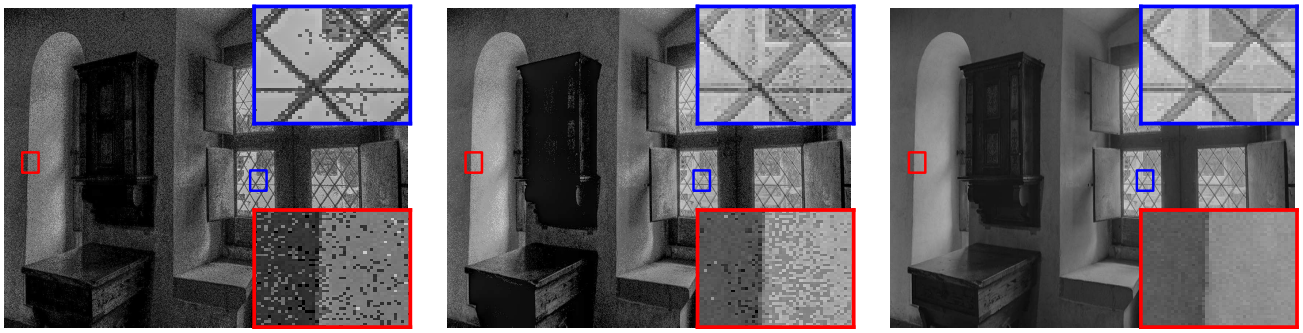

$q = 1$, PSNR $= 17.94$ dB $q = 16$, PSNR $= 20.77$ dB Proposed, PSNR $= 31.46$ dB

Fig. 11. The reconstructed HDR images using different thresholds. See supplementary material for additional results.

range extension method discussed in Section IV-D. When different threshold schemes are used, the reconstructed HDR images will be affected. The objective of this experiment is to evaluate the influence of the threshold in HDR imaging.

In this experiment, we consider the HDR-Eye image dataset [46], [47]. Each HDR image in this dataset contains 9 images acquired at different exposure settings (-2.7,-2, -1.3, -0.7, 0, 0.7, 1.3, 2, and 2.7 EV). A snapshot of these images are shown in Figure 10. From each exposure, we simulate the photon counts resulting from the luminance channel. The sensor gain is set as $\alpha = K^2(q_{\max} - 1)$ to ensure proper number of photons, where $K = 4 \times 4 = 16$ and $q_{\max} = 16$. On the reconstruction side, we reconstruct the 9 images using the MLE discussed in Section III-A. Then, we apply the standard tone mapping algorithm [48], [49] to fuse the 9 images into one single image. As a reference, we apply the same tone mapping and fusion algorithm to the 9 ground truth images. PSNR between the reference and the estimated is then recorded.

The result of this experiment is shown in Figure 11. With the proposed threshold update scheme, the reconstructed images achieve the highest PSNR value and visual quality. When $q = 1$, which is too low, the image appears under-exposed. When $q = 16$, which is too high, the image appears over-exposed. The spatially varying property of the proposed method mitigates the issue by allowing multiple thresholds.

As for comparison with the existing HDR imaging methods using CMOS, we argue that the major difference would be the total amount of data acquisition time. However, a fair comparison can only be made when an actual QIS becomes available for the experiment. We are optimistic about the QIS hardware development, and we believe such experimental results can be demonstrated in a near future.

VI. Conclusion

Quanta Image Sensor is a new image sensor for high speed, high resolution and high dynamic range imaging. The sensor has a threshold which needs to be carefully adjusted so that the dynamic range can be maximized. We studied the threshold design problem by establishing several theoretical results. First, we showed that an oracle threshold can be obtained assuming that we know the underlying pixel value. Our result showed that the oracle threshold must match with the pixel value in order to maximize the signal to noise ratio. Second, we showed that around the oracle threshold, there exists a set of thresholds that can produce asymptotically unbiased estimates of the pixel value. Within this set of threshold, the signal to noise ratio stays very close to the oracle case. Third, we developed a bisection method to update the threshold scheme. Experimental results showed the effectiveness of our proposed approach compared to the standard approach that uses fixed threshold for all pixels.

Acknowledgment

The authors thank Professor Eric Fossum, Jiaju Ma and Saleh Masoodian at Dartmouth College for many insightful discussions about the physics and circuits of QIS.

Appendix A

A. Proof of Proposition 3

The Fisher Information metric is defined as:

$$I_q(c) \stackrel{\text{def}}{=} \mathbb{E}_B \left[\frac{-\partial^2}{\partial c^2} \log \mathbb{P}(B = b; \theta, q) \right], \tag{22}$$

where $\theta = \alpha c / K$. Using the chain rule, we can derive the Fisher Information as follows

$$I_q(c) = \left(\frac{\alpha}{K}\right)^2 \mathbb{E}_B \left[\frac{-\partial^2}{\partial \theta^2} \log \mathbb{P}(B = b; \theta, q) \right]. \tag{23}$$

The expectation can be calculated as follows

$$\begin{aligned} I_q(c) = &\left(\frac{\alpha}{K}\right)^2 \left[\frac{-\partial^2}{\partial \theta^2} \log \mathbb{P}(B = 1; \theta, q) \right] \mathbb{P}(B = 1; \theta, q) \\ &+ \left(\frac{\alpha}{K}\right)^2 \left[\frac{-\partial^2}{\partial \theta^2} \log \mathbb{P}(B = 0; \theta, q) \right] \mathbb{P}(B = 0; \theta, q) \end{aligned} \tag{24}$$

Using (7) to differentiate the 1st term, we get:

$$\frac{\partial^2}{\partial\theta^2}\log\mathbb{P}(B=1;\theta,q)=\frac{\partial^2}{\partial\theta^2}\log\left(1-\Psi_q(\theta)\right)$$
$$=\frac{R'(1-\Psi_q(\theta))-R^2/\Gamma(q)}{\Gamma(q)\left(1-\Psi_q(\theta)\right)^2}, \tag{25}$$

where $R=e^{-\theta}\theta^{q-1}$ and $R'=\partial R/\partial\theta$. Similarly, the second term is

$$\frac{\partial^2}{\partial\theta^2}\log\mathbb{P}(B=0;\theta,q)=\frac{\partial^2}{\partial\theta^2}\log\Psi_q(\theta)$$
$$=-\frac{R'\Psi_q(\theta)+R^2/\Gamma(q)}{\Gamma(q)\left(\Psi_q(\theta)\right)^2}. \tag{26}$$

Substitute (25) and (26) in (24) yields

$$I_q(\theta)=\left(\frac{\alpha}{K}\right)^2\Big[-\frac{R'\Gamma(q)(1-\Psi_q(\theta))-R^2}{\Gamma^2(q)\left(1-\Psi_q(\theta)\right)}$$
$$+\frac{R'\Gamma(q)\Psi_q(\theta)+R^2}{\Gamma^2(q)\Psi_q(\theta)}\Big]$$
$$=\left(\frac{\alpha}{K}\right)^2\frac{e^{-2\theta}\theta^{2q-2}}{\Gamma^2(q)\Psi_q(\theta)\left(1-\Psi_q(\theta)\right)}.$$

B. Proof of Proposition 4

The lower bound is obtained by observing that the product $\Psi_q(\theta)\left(1-\Psi_q(\theta)\right)$ attains its maximum value when $\Psi_q(\theta)=1/2$. Substituting with the upper bound $\Psi_q(\theta)\left(1-\Psi_q(\theta)\right)\le 1/4$, we get:

$$\log(c^2I_q(c))=\log\left\{\left(\frac{\alpha c}{K}\right)^2\frac{e^{-2\theta}\theta^{2q-2}}{\Gamma^2(q)\Psi_q(\theta)\left(1-\Psi_q(\theta)\right)}\right\}$$
$$=\log\frac{e^{-2\theta}\theta^{2q}}{\Gamma^2(q)\Psi_q(\theta)\left(1-\Psi_q(\theta)\right)}$$
$$\ge\log\frac{4e^{-2\theta}\theta^{2q}}{\Gamma^2(q)}$$
$$=2\log 2-2\theta+2q\log\theta-2\log\Gamma(q)$$
$$=2\left(\log 2-\frac{\alpha c}{K}+q\log\frac{\alpha c}{K}-\log\Gamma(q)\right).$$

C. Proof of Proposition 5

Using the definition of Gamma function $\Gamma(q)=(q-1)!$ and $\theta=\frac{\alpha c}{K}$, we can rewrite the lower bound in Proposition 4 as follows.

$$L_q(c)=2\left(\log 2-\theta+q\log\theta-\log(q-1)!\right)$$
$$=2\left(\log 2-\theta+(q-1)\log\theta+\log\theta-\log\prod_{k=1}^{q-1}k\right)$$
$$=2\left(\log 2-\theta+\sum_{k=1}^{q-1}\log(\theta/k)+\log\theta\right)$$

The only dependence on q is in the second term, so we take a closer look at it. When $q-1<\lfloor\theta\rfloor$, all summands $\log(\theta/k)$ are positive because $k<\lfloor\theta\rfloor$. Hence, the total sum increases by increasing q. On the other hand, when $q-1>\lfloor\theta\rfloor$, we start to add negative summands $\log(\theta/k)$ because $k>\theta$. Therefore, the total sum decreases on increasing $q-1$ over $\lfloor\theta\rfloor$. Thus, maximum is obtained at $q=\lfloor\theta\rfloor+1=\lfloor\frac{\alpha c}{K}\rfloor+1$.

D. Proof of Proposition 6

By definition, $S\overset{\text{def}}{=}\sum_{t=0}^{T-1}\sum_{k=0}^{K-1}B_{k,t}$ is the summation of KT independent i.i.d. Bernoulli random variables. Therefore, S is a binomial random variable with parameters $n\overset{\text{def}}{=}KT$ and $p\overset{\text{def}}{=}1-\Psi(\alpha c/K)$. The mean and variance of a binomial random variable is $\mathbb{E}[S]=np$, and $\mathrm{Var}[S]=np(1-p)$. Therefore, we have

$$\mathbb{E}\left[\gamma_q(c)\right]=1-\frac{\mathbb{E}[S]}{KT}=\Psi_q\left(\frac{\alpha c}{K}\right),\quad\text{and}$$
$$\mathrm{Var}\left[\gamma_q(c)\right]=\frac{\mathrm{Var}\left[S\right]}{K^2T^2}=\frac{1}{KT}\Psi_q\left(\frac{\alpha c}{K}\right)\left(1-\Psi_q\left(\frac{\alpha c}{K}\right)\right).$$

E. Proof of Proposition 7

The probability $\mathbb{P}[0<\gamma_q(c)<1]$ can be evaluated by checking the complement when $\gamma_q(c)=0$ or $\gamma_q(c)=1$:

$$\mathbb{P}[0<\gamma_q(c)<1]=1-\mathbb{P}[\gamma_q(c)=0]-\mathbb{P}[\gamma_q(c)=1]$$
$$=1-\mathbb{P}[S=0]-\mathbb{P}[S=KT]$$
$$\overset{(a)}{=}1-\Psi_q(\theta)^{KT}-[1-\Psi_q(\theta)]^{KT},$$

where (a) follows from the fact that S, which is a sum of i.i.d. Bernoulli random variables, is a binomial random variable.

Let $0<\delta<1$. If

$$1-\left(\frac{\delta}{2}\right)^{\frac{1}{KT}}\le\Psi_q(\theta)\le\left(\frac{\delta}{2}\right)^{\frac{1}{KT}},$$

then we have

$$\Psi_q(\theta)^{KT}<\frac{\delta}{2}\ \text{ and }\ [1-\Psi_q(\theta)]^{KT}<\frac{\delta}{2}.$$

Thus, it holds that

$$1-\Psi_q(\theta)^{KT}-[1-\Psi_q(\theta)]^{KT}>1-\delta.$$

REFERENCES

[1] E. R. Fossum, "What to do with sub-diffraction-limit (SDL) pixels?–A proposal for a gigapixel digital film sensor (DFS)," in *Proc. IEEE Workshop CCDs Adv. Image Sensors*, Sep. 2005, pp. 214–217.

[2] J. Ma, D. Hondongwa, and E. R. Fossum, "Jot devices and the quanta image sensor," in *Proc. IEEE Int. Electron Devices Meeting*, Dec. 2014, pp. 10.1.1–10.1.4.

[3] J. Ma and E. R. Fossum, "A pump-gate jot device with high conversion gain for a quanta image sensor," *IEEE J. Electron Devices Soc.*, vol. 3, no. 2, pp. 73–77, Mar. 2015.

[4] J. Ma, L. Anzagira, and E. R. Fossum, "A 1 μm-pitch quanta image sensor jot device with shared readout," *IEEE J. Electron Devices Soc.*, vol. 4, no. 2, pp. 83–89, Mar. 2016.

[5] F. Yang, Y. M. Lu, L. Sbaiz, and M. Vetterli, "An optimal algorithm for reconstructing images from binary measurements," in *Proc. IS&T/SPIE Electronic Imaging, Computational Imaging VIII*, Jan. 2010, vol. 7533, pp. 75330K–75330K–12.

[6] F. Yang, Y. M. Lu, L. Sbaiz, and M. Vetterli, "Bits from photons: Oversampled image acquisition using binary poisson statistics," *IEEE Trans. Image Process.*, vol. 21, no. 4, pp. 1421–1436, Apr. 2012.

[7] S. H. Chan and Y. M. Lu, "Efficient image reconstruction for gigapixel quantum image sensors," in *Proc. IEEE Global Conf. Signal and Information Processing (GlobalSIP'14)*, Dec. 2014, pp. 312–316.

[8] O. A. Elgendy and S. H. Chan, "Image reconstruction and threshold design for quanta image sensors," in *Proc. IEEE Int. Conf. Image Process. (ICIP'16)*, Sep. 2016, pp. 978–982.

[9] S. H. Chan, O. A. Elgendy, and X. Wang, "Images from bits: Non-iterative image reconstruction for quanta image sensors," *MDPI Sensors*, vol. 16, no. 11, pp. 1961, 2016.

[10] E. R. Fossum, J. Ma, and S. Masoodian, "Quanta image sensor: concepts and progress," in *Proc. SPIE 9858, Advanced Photon Counting Techniques X*, 2016, vol. 9858, pp. 985804–985804–14.

[11] I. M. Antolovic, S. Burri, C. Bruschini, R. Hoebe, and E. Charbon, "Nonuniformity analysis of a 65k pixel CMOS SPAD imager," *IEEE Trans. Electron Devices*, vol. 63, no. 1, pp. 57–64, Jan. 2016.

[12] "Andor ixon ultra 888 specifications," http://www.andor.com/pdfs/specifications/iXon_Ultra_888_EMCCD_Specifications.pdf, Accessed: 2016-08-03.

[13] B. F. Aull, D. R. Schuette, D. J. Young, D. M. Craig, B. J. Felton, and K. Warner, "A study of crosstalk in a 256×256 photon counting imager based on silicon Geiger-mode avalanche photodiodes," *IEEE Sens. J.*, vol. 15, no. 4, pp. 2123–2132, Apr. 2015.

[14] N. A. W. Dutton, I. Gyongy, L. Parmesan, and R. K. Henderson, "Single photon counting performance and noise analysis of CMOS SPAD-based image sensors," *MDPI Sensors*, vol. 16, no. 7, pp. 1122, Jul. 2016.

[15] S. Masoodian, A. Rao, J. Ma, K. Odame, and E. R. Fossum, "A 2.5 pj/b binary image sensor as a pathfinder for quanta image sensors," *IEEE Trans. Electron Devices*, vol. 63, no. 1, pp. 100–105, Jan. 2016.

[16] F. Yang, *Bits from Photons: Oversampled Binary Image Acquisition*, Ph.D. thesis, École Polytechnique Fédérale De Lausanne, 2012.

[17] Y. M. Lu, "Adaptive sensing and inference for single-photon imaging," in *Proc. 47th Annual Conf. Inf. Sci. and Sys. (CISS'13)*, Mar. 2013, pp. 1–6.

[18] C. Hu and Y. M. Lu, "Adaptive time-sequential binary sensing for high dynamic range imaging," in *Proc. SPIE Conf. Adv. Photon Counting*, 2012, vol. 8375, pp. 83750A–1.

[19] T. Vogelsang and D. G. Stork, "High-dynamic-range binary pixel processing using non-destructive reads and variable oversampling and thresholds," in *Proc. IEEE Sens*, Oct. 2012, pp. 1–4.

[20] T. Vogelsang, M. Guidash, and S. Xue, "Overcoming the full well capacity limit: high dynamic range imaging using multi-bit temporal oversampling and conditional reset," in *Proc. Int. Image Sens. Workshop (IISW)*, Snowbird, UT, 2013.

[21] T. Vogelsang, D. G. Stork, and M. Guidash, "Hardware validated unified model of multibit temporally and spatially oversampled image sensors with conditional reset," *J. Electronic Imaging*, vol. 23, no. 1, pp. 013021, 2014.

[22] J. Hynecek, "Impactron-a new solid state image intensifier," *IEEE Trans. Electron Devices*, vol. 48, no. 10, pp. 2238–2241, Oct. 2001.

[23] M. S. Robbins and B. J. Hadwen, "The noise performance of electron multiplying charge-coupled devices," *IEEE Trans. Electron Devices*, vol. 50, no. 5, pp. 1227–1232, May 2003.

[24] N. A. W. Dutton, I. Gyongy, L. Parmesan, S. Gnecchi, N. Calder, B. R. Rae, S. Pellegrini, L. A. Grant, and R. K. Henderson, "A SPAD-based QVGA image sensor for single-photon counting and quanta imaging," *IEEE Trans. Electron Devices*, vol. 63, no. 1, pp. 189–196, Jan. 2016.

[25] L. Liang, H. Shen, P. De Camilli, and J. S. Duncan, "A novel multiple hypothesis based particle tracking method for clathrin mediated endocytosis analysis using fluorescence microscopy," *IEEE Trans. Image Process.*, vol. 23, no. 4, pp. 1844–1857, Apr. 2014.

[26] L. H. C. Braga, L. Gasparini, L. Grant, R. K. Henderson, N. Massari, M. Perenzoni, D. Stoppa, and R. Walker, "A fully digital 8×16 SiPM array for PET applications with per-pixel TDCs and real-time energy output," *IEEE J. Solid-State Circuits*, vol. 49, no. 1, pp. 301–314, Jan. 2014.

[27] S. P. Poland, N. Krstajić, J. Monypenny, S. Coelho, D. Tyndall, R. J. Walker, V. Devauges, J. Richardson, N. Dutton, P. Barber, D. D. Li, K. Suhling, T. Ng, R. K. Henderson, and S. M. Ameer-Beg, "A high speed multifocal multiphoton fluorescence lifetime imaging microscope for live-cell fret imaging," *Biomed. Opt. Express*, vol. 6, no. 2, pp. 277–296, Feb. 2015.

[28] G. Grubbs, R. Michell, M. Samara, D. Hampton, and J.-M. Jahn, "A synthesis of star calibration techniques for ground-based narrowband electron-multiplying charge-coupled device imagers used in auroral photometry," *J. Geophysical Research: Space Physics*, vol. 121, no. 6, pp. 5991–6002, 2016, 2015JA022186.

[29] P. Seitz and A. J. Theuwissen, *Single-photon imaging*, vol. 160, Springer Science & Business Media, 2011.

[30] L. J. Meng, "An intensified EMCCD camera for low energy Gamma ray imaging applications," *IEEE Trans. Nuclear Science*, vol. 53, no. 4, pp. 2376–2384, Aug. 2006.

[31] D. Shin, F. Xu, D. Venkatraman, R. Lussana, F. Villa, F. Zappa, V. K. Goyal, F. N. C. Wong, and J. H. Shapiro, "Photon-efficient imaging with a single-photon camera," *Nature Communications*, vol. 7, pp. –, 2016.

[32] S. Burri, Y. Maruyama, X. Michalet, F. Regazzoni, C. Bruschini, and E. Charbon, "Architecture and applications of a high resolution gated spad image sensor," *Opt. Express*, vol. 22, no. 14, pp. 17573–17589, July 2014.

[33] E Amri, Y. Felk, D. Stucki, J. Ma, and E. R. Fossum, "Quantum random number generation using a quanta image sensor," *MDPI Sensors*, vol. 16, no. 7, pp. 1002, Jun. 2016.

[34] E. R. Fossum, "The Quanta Image Sensor (QIS): Concepts and Challenges," in *Proc. OSA Topical Mtg Computational Optical Sensing and Imaging*, Jul. 2011, paper JTuE1.

[35] J. Ma and E. R. Fossum, "Quanta image sensor jot with sub 0.3e- r.m.s. read noise and photon counting capability," *IEEE Electron Device Letters*, vol. 36, no. 9, pp. 926–928, Sep. 2015.

[36] L. Sbaiz, F. Yang, E. Charbon, S. Susstrunk, and M. Vetterli, "The gigavision camera," in *Proc. 2009 IEEE Int. Conf. Acoustics, Speech and Signal Processing (ICASSP'09)*, Apr. 2009, pp. 1093–1096.

[37] F. Yang, L. Sbaiz, E. Charbon, S. Süsstrunk, and M. Vetterli, "On pixel detection threshold in the gigavision camera," in *Proc. IS&T/SPIE Electronic Imaging, Digital Photography VI*, 2010, vol. 7537, pp. 75370G–75370G–8.

[38] N. A. W. Dutton, L. Parmesan, A. J. Holmes, L. A. Grant, and R. K. Henderson, "320 $\times$ 240 oversampled digital single photon counting image sensor," in *Proc. Symp VLSI Circuits*, Jun. 2014, pp. 1–2.

[39] I. M. Antolovic, S. Burri, R. A. Hoebe, Y. Maruyama, C. Bruschini, and E. Charbon, "Photon-counting arrays for time-resolved imaging," *MDPI Sensors*, vol. 16, no. 7, pp. 1005, 2016.

[40] M. Abramowitz and I. A. Stegun, *Handbook of Mathematical Functions: with Formulas, Graphs, and Mathematical Tables*, Number 55. Courier Corporation, 1964.

[41] F. Yang, L. Sbaiz, E. Charbon, S. Ssstrunk, and M. Vetterli, "Image reconstruction in the gigavision camera," in *Proc. IEEE 12th Int. Conf. on Computer Vision Workshops (ICCV Workshops), 2009*, Sep. 2009, pp. 2212–2219.

[42] E. R. Fossum, "Modeling the performance of single-bit and multi-bit quanta image sensors," *IEEE J. Electron Devices Soc.*, vol. 1, no. 9, pp. 166–174, Sep. 2013.

[43] I. Sprow, D. Kuepper, Z. Barańczuk, and P. Zolliker, "Image quality assessment using a high dynamic range display," in *Proc. 12th Congress of the International Colour Association, Newcastle upon Tyne, England*, Jul. 2013.

[44] S. Hasinoff, D. Sharlet, R. Geiss, A. Adams, J. T. Barron, F. Kainz, J. Chen, and M. Levoy, "Burst photography for high dynamic range and low-light imaging on mobile cameras," *ACM Transactions on Graphics (Proc. SIGGRAPH Asia)*, 2016.

[45] D. Martin, C. Fowlkes, D. Tal, and J. Malik, "A database of human segmented natural images and its application to evaluating segmentation algorithms and measuring ecological statistics," in *Proc. 8th Int. Conf. Computer Vision*, July 2001, vol. 2, pp. 416–423.

[46] "HDR-eye dataset," http://mmspg.epfl.ch/hdr-eye, Accessed: 2016-11-30.

[47] H. Nemoto, P. Korshunov, P. Hanhart, and T. Ebrahimi, "Visual attention in LDR and HDR images," in *9th Int. Workshop on Video Process. and Quality Metrics for Consumer Electronics (VPQM)*, 2015.

[48] T. Mertens, J. Kautz, and F. V. Reeth, "Exposure fusion," in *Proc. 15th Pacific Conf. Comp. Graphics and App., 2007. PG '07.*, Oct 2007, pp. 382–390.

[49] F. Banterle, A. Artusi, K. Debattista, and A. Chalmers, *Advanced high dynamic range imaging: theory and practice*, AK Peters (CRC Press), Natick, MA, USA, 2011.

Optimal Threshold Design for Quanta Image Sensor (Supplementary Material)

Omar A. Elgendy, *Student Member, IEEE* and Stanley H. Chan, *Member, IEEE*

arXiv:1704.03886v1 [cs.CV] 12 Apr 2017

Abstract

This supplementary report provides the following additional information of the main article.

- Derivation of $\mathrm{SNR}_q(c)$ from exposure-referred SNR.
- Properties of the incomplete Gamma function.
- Phase transition under different configurations.
- Additional results for HDR image reconstruction.

I. Derivation of $\mathrm{SNR}_q(c)$ from exposure-referred SNR

In the literature of QIS devices, one metric to quantify the image quality is the *exposure*-referred signal-to-noise [1]. In image processing, however, exposure-referred SNR is not commonly used. The goal of this section is to show that the SNR we showed in the main article is equivalent to the exposure-referred SNR.

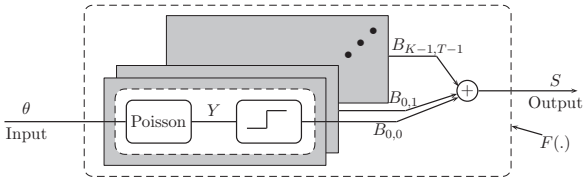

Fig. 1. Block diagram illustrating a QIS with input-output relation output $= F($input$)$

To understand the exposure-referred SNR, we have to first understand two common ways of defining a signal to noise ratio. Consider the truncated Poisson part of the QIS model shown in Figure 1. The input to this model is the over-sampled measurement θ. The truncated Poisson process can be considered as a black box function F which takes an input θ and generates an output S, defined as

$$S = \sum_{t=0}^{T-1} \sum_{k=0}^{K-1} B_{k,t}, \tag{1}$$

where $\mathcal{B}_n = \{B_{k,t} \mid k = 0, 1, \ldots, K-1,\ t = 0, 1, \ldots, T-1\}$ is the spatial-temporal block containing all binary bits corresponding to θ. As shown in the main article, the mean and variance of S are

$$\mathbb{E}[S] = KT(1 - \Psi_q(\theta)), \quad \mathrm{Var}[S] = KT\Psi_q(\theta)(1 - \Psi_q(\theta)), \tag{2}$$

respectively.

The first notion of signal-to-noise, which is the one used in CCD and CMOS, is called the output-referred SNR. $\mathrm{SNR}_{\mathrm{OR}}$ is defined as the ratio between the output signal and the photon shot noise. Referring to Figure 1, this is

$$\mathrm{SNR}_{\mathrm{OR}} = \frac{\text{output signal}}{\text{noise}} = \frac{\mathbb{E}[S]}{\sqrt{\mathrm{Var}[S]}} = \sqrt{KT\frac{1 - \Psi_q(\theta)}{\Psi_q(\theta)}}. \tag{3}$$

However, $\mathrm{SNR}_{\mathrm{OR}}$ fails to work for QIS because the shot noise is arbitrarily small if all bits are 1 or 0. In [1], Fossum called it squeezing of the noise. If we plot $\mathrm{SNR}_{\mathrm{OR}}$ as a function of θ, then we observe that $\mathrm{SNR}_{\mathrm{OR}}$ approaches to infinity as θ grows.

The authors are with the School of Electrical and Computer Engineering, Purdue University, West Lafayette, IN 47907, USA. Email: {oelgendy, stanchan}@purdue.edu.

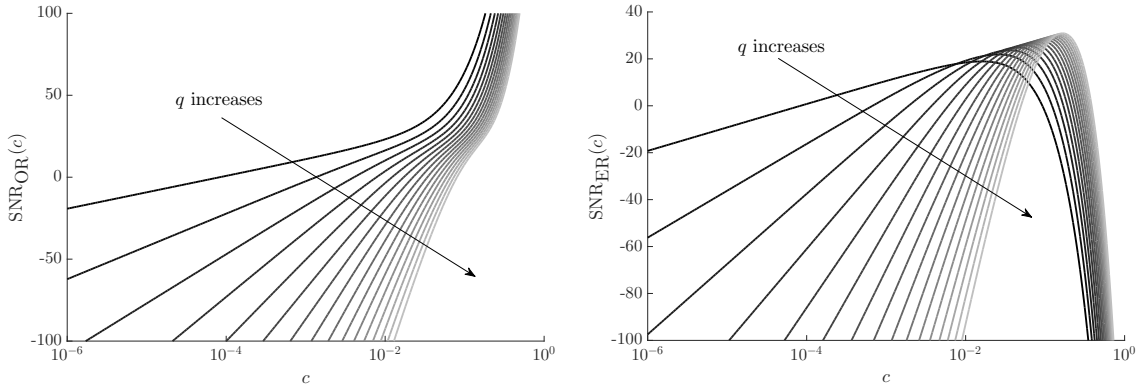

(a) $\mathrm{SNR}_{\mathrm{OR}}$ (b) $\mathrm{SNR}_{\mathrm{ER}}$

Fig. 2. Comparison of the SNRs for $q \in \{1, \ldots, 16\}$. In this experiment, we fix $\alpha = 400$, $K = 4$, and $T = 30$.

The second notion of signal-to-noise, which is a modification of $\mathrm{SNR}_{\mathrm{OR}}$, is the exposure-referred SNR. $\mathrm{SNR}_{\mathrm{ER}}$ is the ratio between the exposure signal θ and the exposure-referred noise. This noise is defined as [1]:

$$\text{Exposure-referred noise} = \frac{d\theta}{d\mathbb{E}[S]}\sqrt{\mathrm{Var}[S]}$$

The factor $\frac{d\theta}{d\mathbb{E}[S]}$ can be considered as the "inverse" transfer function from the output to the input. $\frac{d\theta}{d\mathbb{E}[S]}$ can be determined by taking derivative of the expectation in (2) with respect to $\mathbb{E}[S]$

$$\frac{d\mathbb{E}[S]}{d\mathbb{E}[S]} = \frac{dKT\left(1 - \Psi_q(\theta)\right)}{d\mathbb{E}[S]}$$

Using chain rule, we observe that

$$1 = -KT\frac{d}{d\theta}\Psi_q(\theta)\frac{d\theta}{d\mathbb{E}[S]}$$

Since $\frac{d}{d\theta}\Psi_q(\theta) = \frac{-e^{-\theta}\theta^{q-1}}{\Gamma(q)}$, it holds that

$$1 = -KT\left(\frac{-e^{-\theta}\theta^{q-1}}{\Gamma(q)}\right)\frac{d\theta}{d\mathbb{E}[S]}$$

Hence,

$$\frac{d\theta}{d\mathbb{E}[S]} = \frac{\Gamma(q)}{KTe^{-\theta}\theta^{q-1}}$$

The exposure-referred SNR is defined as

$$\begin{aligned}\mathrm{SNR}_{\mathrm{ER}} &= \frac{\text{exposure signal}}{\text{exposure-referred noise}} \\ &= \frac{\theta}{\sqrt{\mathrm{Var}[S]}\frac{d\theta}{d\mathbb{E}[S]}} \\ &= \frac{e^{-\theta}\theta^{q}}{\Gamma(q)}\sqrt{\frac{KT}{\Psi_q(\theta)\big(1 - \Psi_q(\theta)\big)}}.\end{aligned}$$

Taking logarithm shows that $\mathrm{SNR}_{\mathrm{ER}}$ is identical to the SNR derived from the Fisher Information shown in the main article.

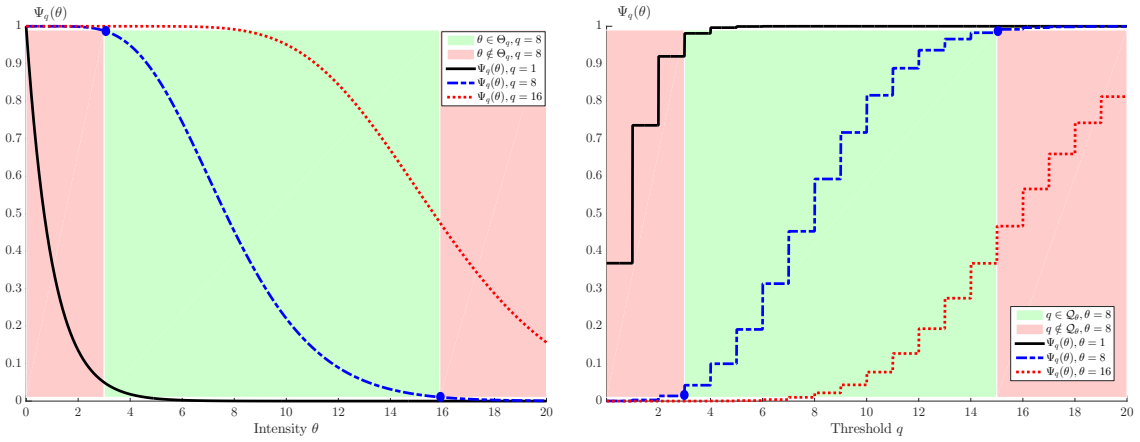

(a) $\Psi_q(\theta)$ vs. θ (b) $\Psi_q(\theta)$ vs. q

Fig. 3. $\Psi_q(\theta)$ as a function of θ and q. In defining, $\mathcal{Q}_\theta$ and Θ_q, we set $\epsilon = 0.01$.

II. Properties of the Incomplete Gamma Function

In the main article, we used the incomplete Gamma function for QIS analysis. In this section, we provide more details about the properties of the incomplete Gamma function.

First, we recall that the normalized upper incomplete Gamma function $\Psi_q : \mathbb{R}^+ \to [0, 1]$ is defined as

$$\Psi_q(\theta) \stackrel{\text{def}}{=} \frac{1}{\Gamma(q)} \int_\theta^\infty t^{q-1} e^{-t} dt, \quad \text{for } \theta > 0,\ q \in \mathbb{N}. \tag{4}$$

where $\Gamma(q) = (q-1)!$ is the standard Gamma function.

In this equation, we note that $\Psi_q(\theta)$ depends on two variables: q and θ.

- As a function of θ. As we showed in the main article, $\Psi_q(\theta)$ is a monotonically decreasing function of θ because the derivative is negative:
$$\frac{d}{d\theta}\Psi_q(\theta) = \frac{-\theta^{q-1}e^{-\theta}}{\Gamma(q)} < 0.$$
However, $\Psi_q(\theta)$ is very close to 1 when θ is small, and is very close to 0 when θ is large. Therefore, there exists a range of θ in which $\Psi_q(\theta)$ can attain a reasonably good inverse. We define this set as the θ-admissible set
$$\Theta_q \stackrel{\text{def}}{=} \{\theta \mid \varepsilon \le \Psi_q(\theta) \le 1 - \varepsilon\}, \tag{5}$$
for any fixed q and a tolerance level ε. An illustration of Θ_q is shown in Figure 3.
- As a function of q. The incomplete Gamma function $\Psi_q(\theta)$ can also be considered as a function of q. In this case, $\Psi_q(\theta)$ is only defined for integer values of q. We illustrate the behavior of $\Psi_q(\theta)$ as a function of q in Figure 3. The set of q in which $\Psi_q(\theta)$ is sufficiently away from 0 and 1 is defined as the q-admissible set.
$$\mathcal{Q}_\theta \stackrel{\text{def}}{=} \{q \mid \varepsilon \le \Psi_q(\theta) \le 1 - \varepsilon\}. \tag{6}$$

III. Phase Transition under Different Configurations

In the main article, we showed the phase transition behavior of the ML estimate using $K = 4$, $T = 50$, and $\delta = 2 \times 10^{-4}$. In this section, we study the effect of changing K, T, and δ on the phase transition region width.

As a function of T. Figure 4-Figure 5 illustrate the phase transition behavior when $T = 10, 25, 50, 100$. As T increases, the width of the green region increases. However, if we fix the range of the bit density $1 - \mathbb{E}[\gamma_q(c)]$, we observe that the SNR does not vary significantly even as T changes.

As a function of K. The spatial oversampling K affects both the threshold $q^*(c) = \lfloor \alpha c/K \rfloor + 1$ and the phase transition width. Figure 6(a) illustrates the behavior of the threshold q^* as a function of K. As K increases, q^* decreases. However, the optimal q^* still stays within the set $\mathcal{Q}_\theta$.

As a function of δ. The constant δ is used to define the set $\mathcal{Q}_\theta$:

$$\mathcal{Q}_\theta \stackrel{\text{def}}{=} \left\{ q \;\middle|\; 1 - \left(\frac{\delta}{2}\right)^{\frac{1}{KT}} \leq \Psi_q(\theta) \leq \left(\frac{\delta}{2}\right)^{\frac{1}{KT}} \right\}. \tag{7}$$

The constant δ is the tolerance level. When δ increases, the size of the set $\mathcal{Q}_\theta$ should also increase. This result is shown in Figure 6(b).

Using the closed form expression of the average bit density $1 - \Psi_q(\theta)$, we can calculate the average bit density at the optimal threshold $q^* = \lfloor \theta \rfloor + 1$, which is shown in Figure 7. We notice that as long as $\theta \geq 1$, the average bit density is between 0.264 and 0.630. Within this range, we observe from Figure 4-Figure 5 that the SNR does not vary significantly if the estimated threshold is deviated from the optimal threshold. This observation relaxes the requirement of the bisection method from obtaining the exact optimal threshold to obtaining a threshold that make the bit density equal to 0.5. Since $0.5 \in [0.264, 0.630]$, we guarantee to achieve an SNR which is sufficiently close to the optimal SNR.

Controlling $\theta \geq 1$ can be achieved by tuning the constant α. Tuning α can be hardware-implemented by increasing the exposure period. Intuitively what $\theta \geq 1$ requires is that the average number of impinging photons per jot must be at least one. If θ is less than one, then most bits will become zeros. Increasing exposure period (i.e., increasing α) will ensure sufficient number of photons.

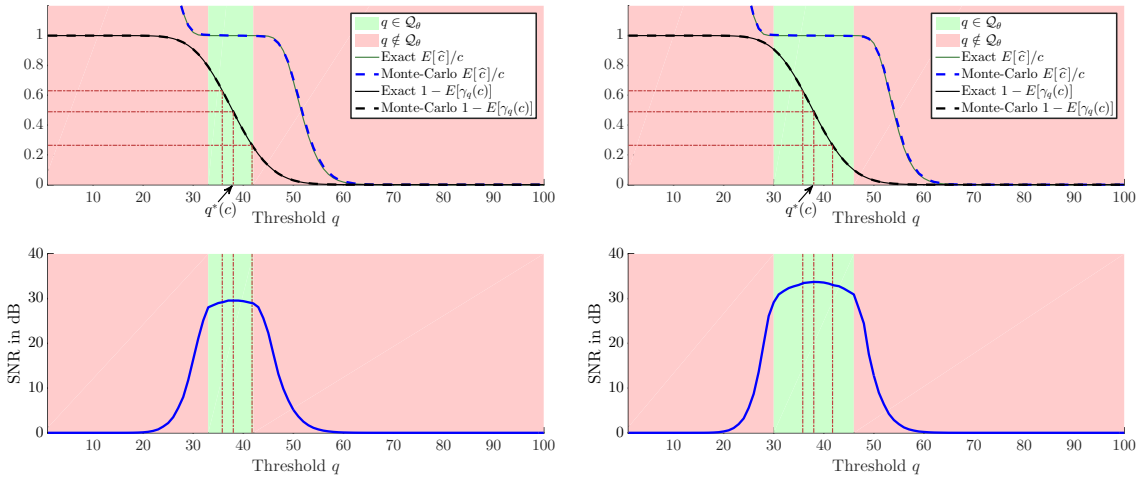

(a) $T = 10$, SNR $\in [28.93, 29.57]$ (b) $T = 25$, SNR $\in [32.98, 33.74]$

Fig. 4. Phase transition for $T = 10$ and $T = 25$. SNR range is shown for average bit density $1 - \mathbb{E}[\gamma_q(c)]$ in the range $[0.264, 0.630]$. For all cases, we set $\delta = 2 \times 10^{-4}$, and $K = 4$.

IV. Supplementary HDR results

In this section, we show more results for HDR image reconstruction using our method compared to the fixed threshold approach. In addition, we compaare with the checkerboard Q-map proposed in [2]. This Q-map is simply an alternation of $q = 1$ and $q = q_{\max}$ in a checkerboard pattern. Figures 8, 9, and 10 show reconstructed HDR images using adapted Q-map by the bisection algorithm, and fixed Q-maps with low threshold ($q = 1$) and high threshold ($q_{\max} = 16$). The spatial and temporal oversampling factors are $K = 4$, and $T = 13$, respectively. Sensor gain is $\alpha = K^2/(q_{\max} - 1)$.

References

[1] E. R. Fossum, "Modeling the performance of single-bit and multi-bit quanta image sensors," *IEEE J. Electron Devices Soc.*, vol. 1, no. 9, pp. 166–174, Sep. 2013.

[2] F. Yang, *Bits from Photons: Oversampled Binary Image Acquisition*, Ph.D. thesis, École Polytechnique Fédérale De Lausanne, 2012.

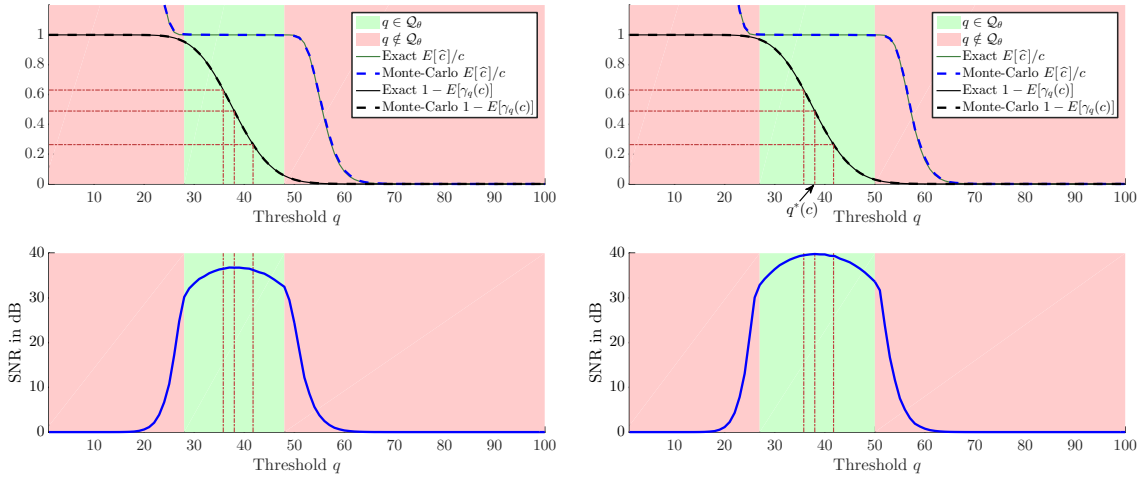

(a) $T = 50$, SNR $\in [36.15, 36.80]$ (b) $T = 100$, SNR $\in [39.35, 39.82]$

Fig. 5. Phase transition for $T = 50$ and $T = 100$. SNR range is shown for average bit density $1 - \mathbb{E}[\gamma_q(c)]$ in the range $[0.264, 0.630]$. For all cases, we set $\delta = 2 \times 10^{-4}$, and $K = 4$.

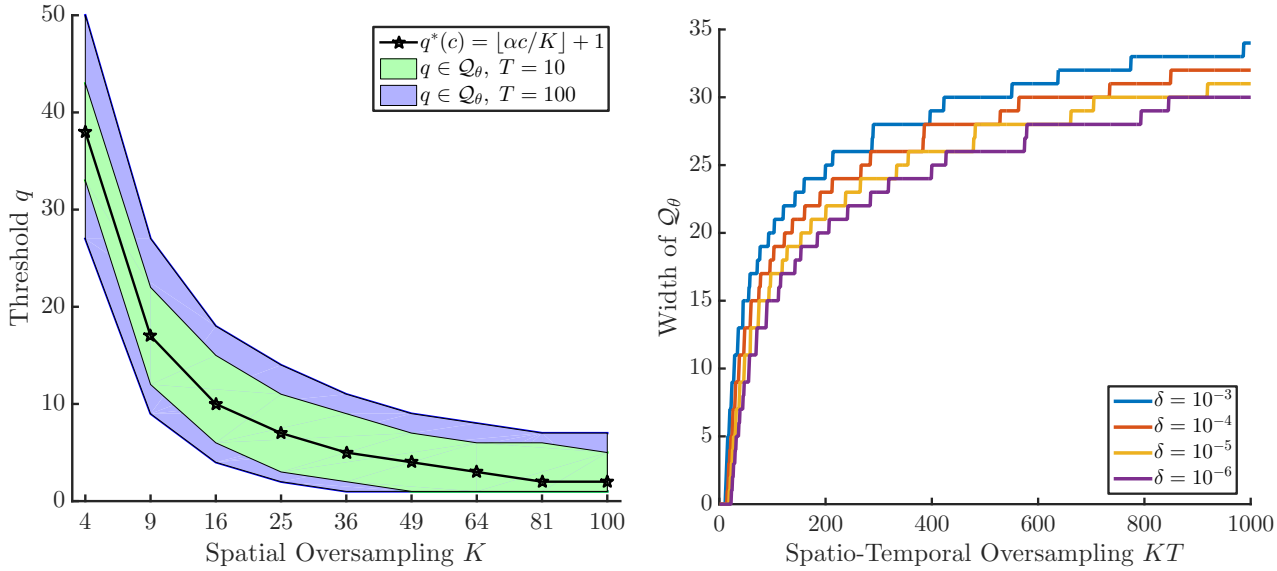

(a) (b)

Fig. 6. (a) The threshold q and $\mathcal{Q}_\theta$ as K increases. (b) The width of $\mathcal{Q}_\theta$ as KT and δ changes.

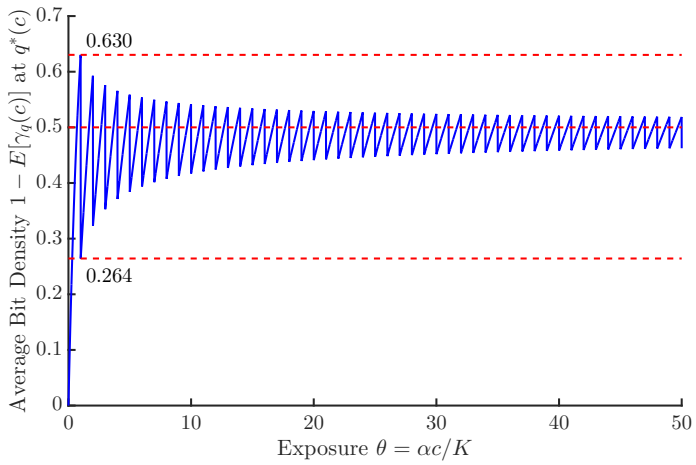

Fig. 7. Average bit density $1 - \mathbb{E}[\gamma_q(c)]$ calculated at optimal threshold $q^* = \lfloor \theta \rfloor + 1$.

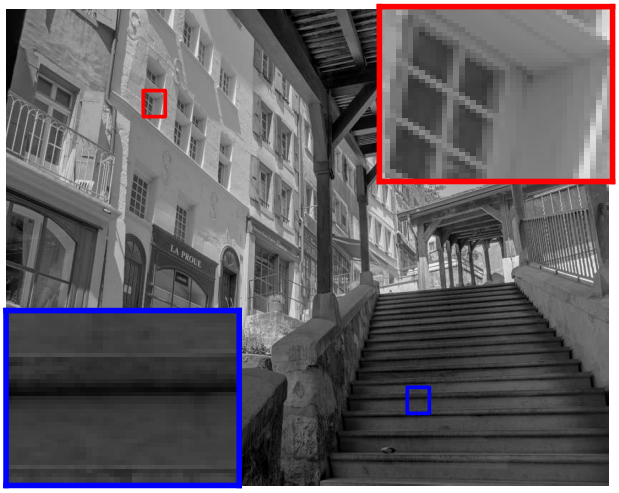

Ground Truth

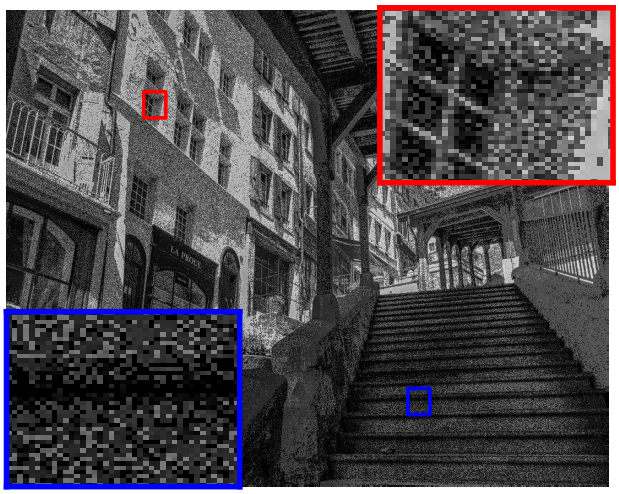

$q = 1$, PSNR $= 15.94$ dB

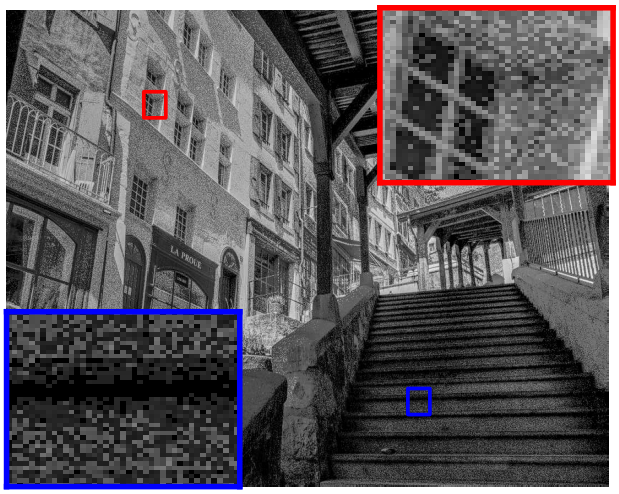

$q = 16$, PSNR $= 20.77$ dB

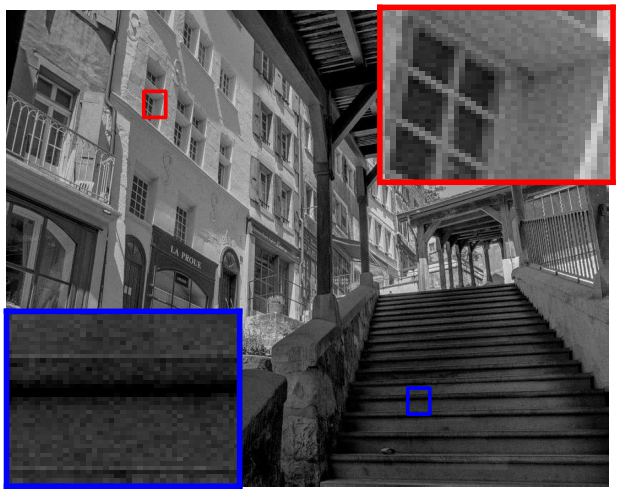

Checkerboard, PSNR $= 24.91$ dB

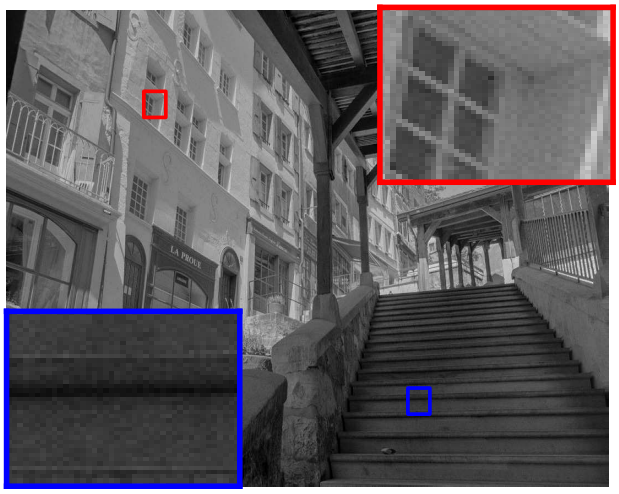

Proposed, PSNR $= 29.97$ dB

Fig. 8. Reconstructed HDR images using different threshold maps

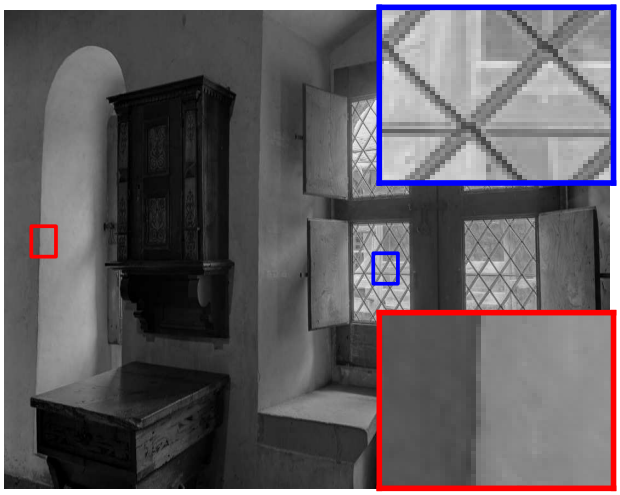

Ground Truth

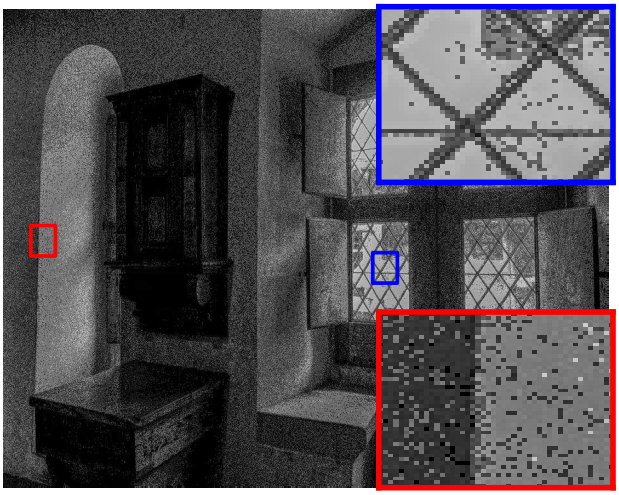

$q = 1$, PSNR $= 17.94$ dB

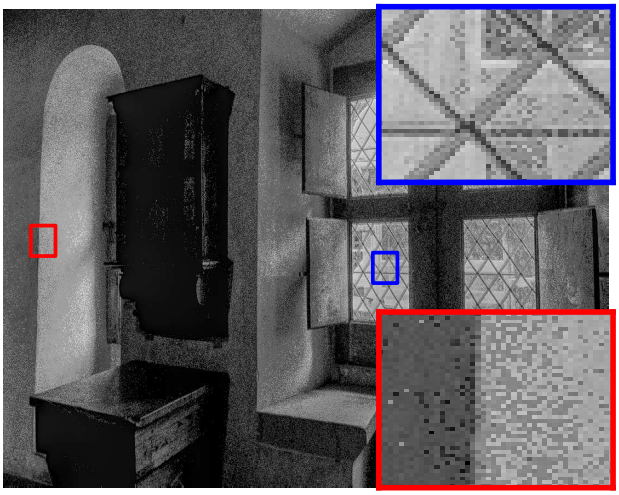

$q = 16$, PSNR $= 20.77$ dB

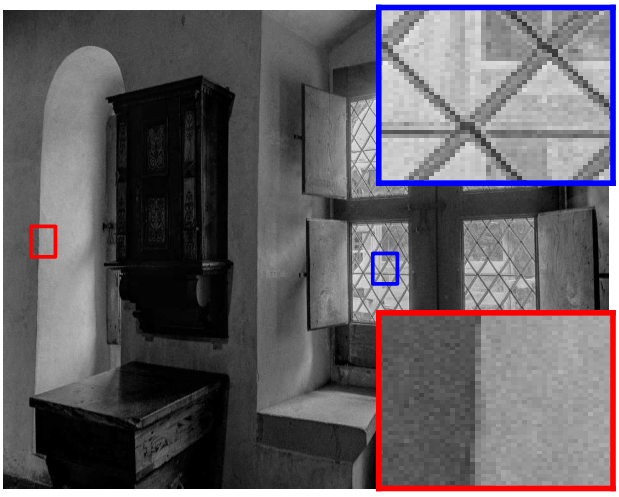

Checkerboard, PSNR $= 28.27$ dB

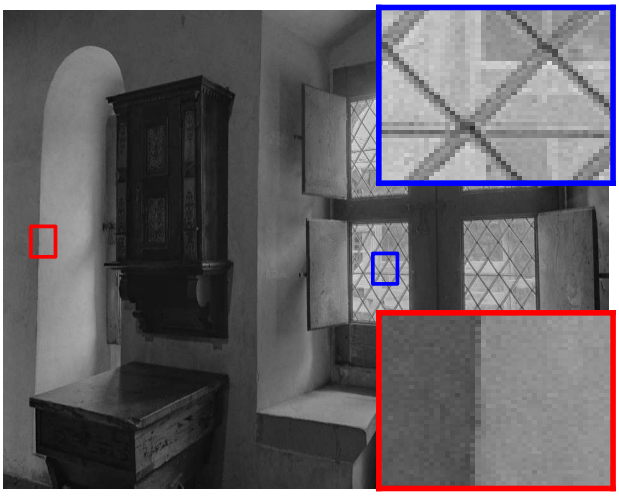

Proposed, PSNR $= 31.46$ dB

Fig. 9. Reconstructed HDR images using different threshold maps

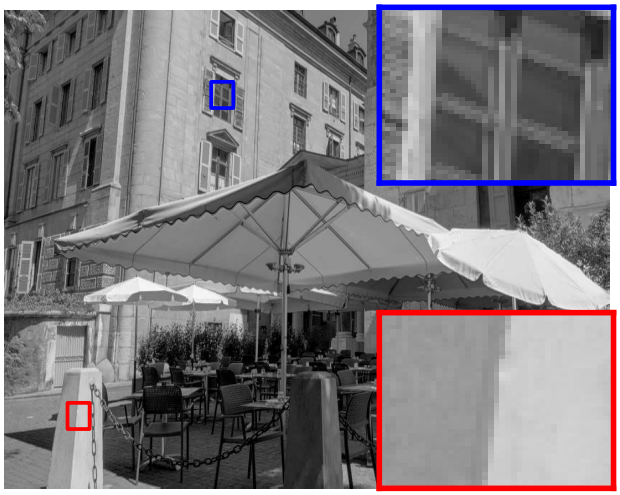

Ground Truth

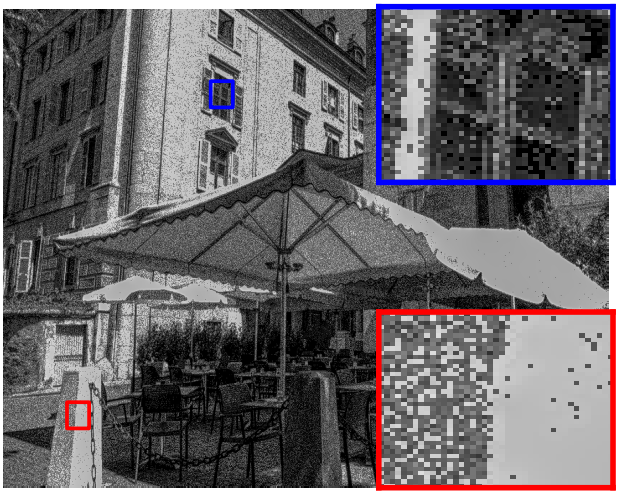

$q = 1$, PSNR $= 15.74$ dB

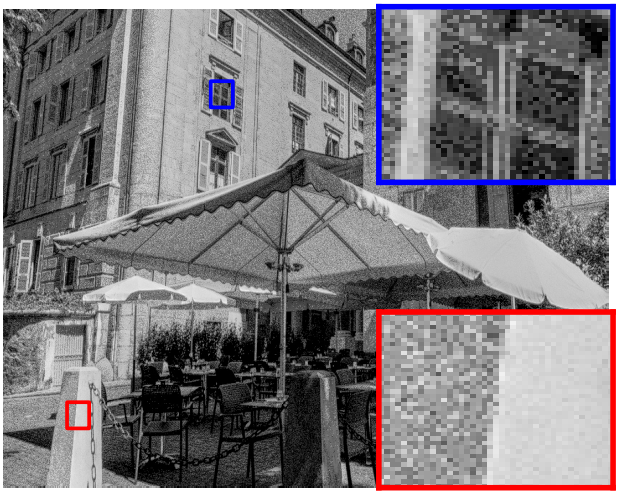

$q = 16$, PSNR $= 20.01$ dB

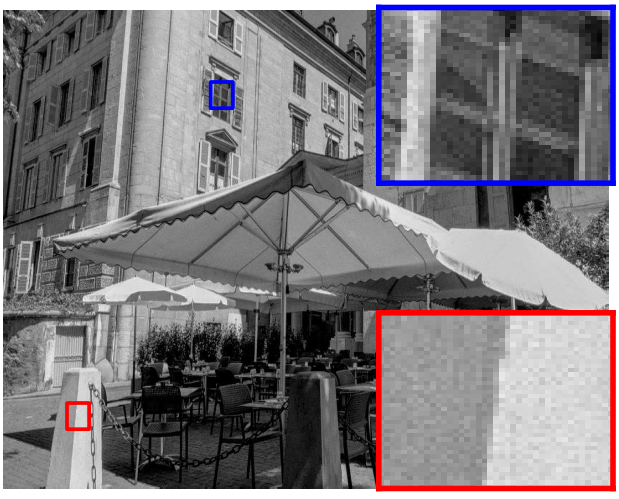

Checkerboard, PSNR $= 27.17$ dB

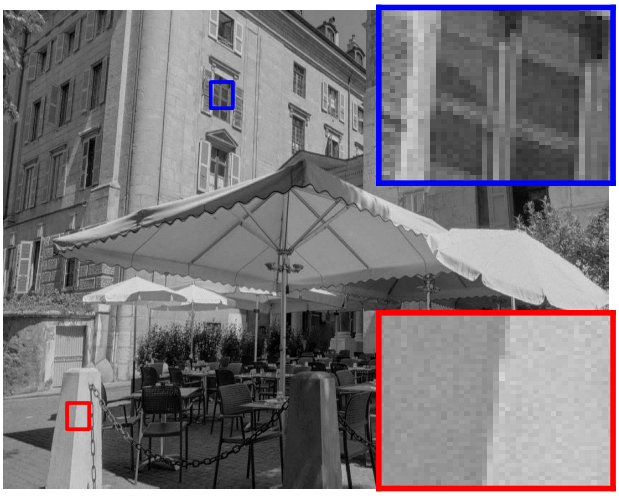

Proposed, PSNR $= 31.65$ dB

Fig. 10. Reconstructed HDR images using different threshold maps